Biogeosciences, 23, 7911–7937, 2026
https://doi.org/10.5194/bg-23-7911-2026
© Author(s) 2026. This work is distributed under
the Creative Commons Attribution 4.0 License.

Biogeosciences Open Access EGU

Tracking sulfate, magnesium and amorphous phases in cultured benthic foraminifera

Guillaume Paris[1], Caroline Thaler[2,3,a], Marc Dellinger[4], Jérôme Aléon[5], Smail Mostefaoui[5], Alice Aléon-Toppani[6], Claire Rollion-Bard[3], David Troadec[7], Guillaume Yangshu Wang[8], and Annachiara Bartolini[2]

[1]Université de Lorraine, CNRS, CRPG, 54000 Nancy, France
[2]CR2P (Centre de Recherche en Paléontologie), UMR 7207 MNHN, CNRS, Sorbonne Université, 75005 Paris, France
[3]Laboratoire des Sciences du Climat et de l'Environnement (LSCE), UMR 8212 CEA, CNRS, Université de Versailles Saint-Quentin en Yvelines, 91191 Gif sur Yvette CEDEX, France
[4]MCAM, UMR 7245 MNHN, CNRS, Sorbonne Université, 75005 Paris, France
[5]Institut de Minéralogie, de Physique des Matériaux et de Cosmochimie (IMPMC), Sorbonne Université, MNHN, CNRS UMR 7590, IRD, 75005 Paris, France
[6]Université Paris-Saclay, CNRS, Institut d'Astrophysique Spatiale, 91405 Orsay, France
[7]Université de Lille, CNRS, Centrale Lille, Junia, Université Polytechnique Hauts de France, UMR 8520-IEMN, 59000 Lille, France
[8]Université Paris Cité, Laboratoire Matériaux et Phénomènes Quantiques UMR 7162, 75205 Paris, France
[a]now at: Bloomineral, 91191 Gif sur Yvette CEDEX, France

Correspondence: Guillaume Paris (guillaume.paris@univ-lorraine.fr)

Received: 17 March 2026 – Discussion started: 26 March 2026
Revised: 8 September 2026 – Accepted: 14 September 2026 – Published: 6 November 2026

Abstract. In this study, we combined high resolution Transmission Electron Microscopy (TEM) bright field and High-Angle Annular Dark-Field Scanning TEM imaging with nanoscale Secondary Ion Mass Spectrometry (NanoSIMS) analyses of *Rosalina* sp. foraminifer cells cultured in ^{33}S-labeled seawater to understand the origin of sulfur in the test and the cytoplasm, its interaction with the ultrastructure of the test and the co-distribution of sulfur with phosphorus, calcium and magnesium. Cells that lived in $^{33}SO_4$-labeled seawater revealed that at least 1/4 of the sulfur observed in the cytoplasm comes from seawater sulfate incorporated during the duration of the growth experiment. Our observations reveal a global co-occurrence of S and Mg within the last two chambers of the test, that all appear more concentrated in two areas, mostly near the Primary Organic Sheet (POS) and in the Outer Calcitic Layer (OCL) that corresponds to the calcite added during the growth of the last chamber. Less crystalline grains can be found in the S and Mg-richest part of the POS and within OCLs. We interpret these grains as a non-crystalline phase likely containing Amorphous Calcium Carbonate (ACC) and organic matter, formed or assembled at the sites of calcification, revealing a complex interplay between S, Mg and Ca. Labeled sulfur is also found within smaller vesicles in the cytoplasm and represents overall 10 % to 25 % of the sulfur we observe. Though we cannot confirm the occurrence of an assimilatory pathway for sulfur in foraminifera, the clear presence of seawater sulfate in the cell demonstrates that sulfate is involved in many aspects of foraminifer biological activity, in close association with Ca-transportation, Mg distribution, and likely with ACC formation and its evolution to calcite.

1 Introduction

Sulfate (SO_4^{2-}) is the second most abundant anion in the modern ocean, ($\sim 28\,\mathrm{mmol\,L^{-1}}$), though its concentration fluctuated massively over Earth's history (e.g. Timofeeff et al., 2001; Horita et al., 2002; Crowe et al., 2014; Fakhraee et al., 2018; LaFlamme et al., 2021). Sulfur has four stable isotopes (^{32}S, ^{33}S, ^{34}S and ^{36}S) and the sulfur isotopic ratio of the most abundant isotopes is homogeneous in the

modern ocean ($\delta^{34}S_{sw} \approx 21‰$) (Craddock et al., 2008; Paris et al., 2013; Rees et al., 1978; Tostevin et al., 2014), where $\delta^{34}S = [(^{34}S/^{32}S_{sample}/^{34}S/^{32}S_{reference}) - 1]$. Sulfate plays a major role in anoxic sediments, where microbial sulfate reduction (MSR) is the most important anaerobic pathway through which organic matter is remineralized (Berner and Canfield, 1989; Canfield and Raiswell, 1999; Claypool et al., 1980; Paytan et al., 1998; Present et al., 2020; Rennie et al., 2018). As a result, variations of $\delta^{34}S_{sw}$ over time can help to constrain changes in the sulfur cycle and its links with the carbon and oxygen cycles. Among the available proxies to reconstruct $\delta^{34}S_{sw}$, Carbonate Associated Sulfate (CAS) has become an increasingly popular archive to investigate the Phanerozoic and the Precambrian (e.g. Burdett et al., 1989; Ohkouchi et al., 1999; Kah et al., 2004; Osburn et al., 2015; Gomes et al., 2016; Present et al., 2020), and even the Archean (Paris et al., 2014b, 2020).

The use of sulfur isotope ratios measured in CAS extracted from biogenic carbonates has sparked the debate of the nature of the phase bearing sulfur in biogenic calcite (e.g. Cuif et al., 2003; Dauphin et al., 2003, 2005, 2013; Cusack et al., 2008; Richardson et al., 2019b). CAS is sulfate inorganically incorporated within the crystal lattice of calcium carbonates (Fernández-Díaz et al., 2010; Kampschulte et al., 2001; Paris et al., 2014a). Over the last decades, sulfur isotopes from CAS from inorganic and most biogenic carbonates have been shown to display small fractionations ($-1‰$ to $+4‰$) from the fluid from which they grew (Barkan et al., 2020; Bryant et al., 2023; Paris et al., 2014a; Rennie et al., 2018; Thaler et al., 2023), and small scale variability ($\approx 1‰$–$3‰$) can be found, in brachiopods shells or coral skeletons (He et al., 2024; Present et al., 2015). However, sulfur is common in organic matter as well (Oae, 2012), and, in biocalcifying rotaliid foraminifera, its global isotopic signature is distinct from that of the sulfate directly incorporated into calcite (e.g. Thaler et al., 2023). Knowing sulfur location, speciation and origin is indeed important to better understand the CAS archive, including CAS from calcitic foraminifer tests, that are one of the most used archive for reconstructions of paleoenvironmental conditions (e.g. Rennie et al., 2018; The Cenozoic CO_2 Proxy Integration Project (CenCO2PIP) Consortium et al., 2023). In addition, sulfur speciation may impact how the original signal is preserved during diagenesis (Richardson et al., 2021).

More generally, sulfate is a critical anion in biogenic calcite formation for three reasons. First, sulfate plays a role in the precipitation of calcite vs. aragonite (Bots et al; 2011, Barkan et al., 2020): at high sulfate concentrations, such as in modern seawater, calcite precipitation is inhibited. Second, the physiological activity of foraminifera requires sulfate, as shown by the death of benthic foraminifera cultivated in sulfate-free or -poor artificial seawater (Thaler et al., 2023). This is coherent with the need for sulfur in organic matter, but other reasons could explain the need for sulfate, such as sulfate assimilation. In eukaryotes, the presence of a sulfate reduction pathway, generally assumed to be restricted to photosynthetic cells (Patron et al., 2008; Schiff, 1980), though intracellular assimilatory sulfate reduction has been proposed to occur in foraminifera (Jauffrais et al., 2019; LeKieffre et al., 2022; Nomaki et al., 2016). Thus, reduced sulfur could be provided by food or through seawater sulfate reduction. Third, sulfur also occurs as sulfate in organic matter in the test. Sulfate enriched glycosaminoglycans, which are complex polysaccharide molecules constituted of a sequence of amino sugars that are covalently attached to proteins, are thought to act as a template for biomineralization (Angell, 1967; Bé et al., 1979; Dauphin et al., 2008; Falini et al., 1996; Hemleben et al., 1986; Langer, 1992; Spero, 1998; Weiner and Erez, 1984).

Such processes may occur also in *Rotaliida*, the most diversified order of biocalcifying foraminifera in the ocean and includes both benthic and planktic species. The distribution of sulfur in their tests, like many other elements such as P and Mg, is characterized by well-documented banding structures at the micron or sub-micron scales, (van Dijk et al., 2019a; Eggins et al., 2004; Fehrenbacher et al., 2017; Geerken et al., 2019; Glock et al., 2019; Lemelle et al., 2020; Paris et al., 2014a), which appears to be linked to the multi-layered growth of the test. The initial stage is the formation of a precursor layer, which is proposed to act as an organic template and has been named primary organic membrane, sheet or zone (POM, POS or POZ; Bé et al., 1979; Erez, 2003; Hemleben et al., 1977, 1986; Lemelle et al., 2020; Nagai et al., 2018; de Nooijer et al., 2014; Tyszka et al., 2021). The subsequent stage of wall growth is a bi-directional precipitation of two calcite layers on both side of the POS. The inner calcitic layer (ICL) is precipitated between the inner organic layer (IOL) and the POS, while the outer calcitic layer (OCL) is precipitated between the POS and the outer organic layer (OOL). In the end, the multi-layer nature of the wall results from the successive additions of new chambers, with a new OCL covering the entire test each time that a new chamber is added. Yet, the meaning of this banding depends on the elements investigated.

On the one hand, sulfur and magnesium (co-)bandings are usually interpreted as associated to the inorganic calcium carbonate phase of the test rather than to organic matter (van Dijk et al., 2017; Lorens and Bender, 1980; Paris et al., 2014a; Richardson et al., 2019a; Spero et al., 2015a; Tanaka et al., 2019). Accordingly, Mg has been shown to be solely inorganically substituted for Ca within the calcite mineral lattice, despite changes in Mg/Ca ratio (Branson et al., 2013). On the other hand, shared S and P banding has also been documented and interpreted as reflecting variations in organic matter (OM) within the test, as their distribution patterns closely resemble those observed for organic-rich regions (e.g., Glock et al., 2019; Geerken et al., 2019). Thus, sulfur would reveal the organic linings, consistent with the presence of organically bound sulfate within the organic matter in the test, as well as S-containing amino acids (Dauphin

et al., 2013; Richardson et al., 2019b) and the role of sulfated molecules in biomineralization.

However, this classical view (P, N and S track organic matter, Mg variations are purely inorganic) has been partially challenged over the years. Sulfate, like Mg, is inorganically incorporated in calcite (Busenberg and Plummer, 1985; Kontrec et al., 2004), though high concentration of sulfate – similarly to Mg – inhibits calcite and favors aragonite precipitation (Barkan et al., 2020; Bots et al., 2011). Even though the need for low sulfate to facilitate calcite precipitation could suggest that foraminifera would try to exclude sulfate from the site of biomineralization, the occurrence of inorganic sulfate in biogenic calcite implies that sulfate is still present in the calcifying fluid (van Dijk et al., 2017; Erez, 2003; Paris et al., 2014a; Richardson et al., 2019a; Thaler et al., 2023). Phosphate also is inorganically included in calcite lattice. Even at low phosphate concentrations (few tens of $\mu mol\,L^{-1}$), inorganic experiments show that phosphate can be adsorbed on the surface of the mineral, incorporated into the growing crystal, or precipitated as calcium-phosphate (House and Donaldson, 1986; Plant and House, 2002; Ren et al., 2021). In addition, phosphate ions are also known to inhibit calcite formation (Burton and Walter, 1990; House, 1987; Lin and Singer, 2006), they share thus one more point with magnesium and sulfate. Magnesium, S and P can all be inorganically included in calcium carbonate, and so can nitrate (Gabitov et al., 2026; Hofmann et al., 2016; Kontrec et al., 2004). Finally, enrichment of Mg (and Na) in the POS of *Orbulina universa* has been interpreted as a contribution of organically-carried Mg (Branson et al., 2016), showing that Mg might not be purely inorganically present in the test, suggesting that all three elements can also be associated to another phase than calcite.

In this regard, we try to understand the trajectory of sulfur from seawater sulfate to its incorporation into calcite, as well as the co-distribution of S, P and Mg and the combined roles of those elements in the structuration of the test. The hypothesis is that inorganic sulfate in the test (CAS) as well as the sulfate groups associated with organic molecules come directly from seawater, in which case they could be expected to both have similar isotopic ratios. By contrast, whether it comes directly from food or through assimilatory sulfate reduction if it occurs in the cell, reduced sulfur in organic matter is most likely isotopically different.

To achieve this, we cultivated a *Rosalina* sp. rotaliid benthic foraminifer in artificial seawater in different conditions, including seawater enriched in the rare sulfur isotope ^{33}S or seawater with natural isotope abundances but feeding the foraminifera using ^{33}S-enriched algae. We applied a new protocol for chemically fixing the foraminifera in order to preserve simultaneously the cytoplasm and the test. We then used Nanoscale Secondary Ion Mass Spectrometer (NanoSIMS) to image the distribution of sulfur isotopes in the cell and the growing structure of the foraminiferal test wall at the nanoscale, as well as P and Mg distribution. Combined with high resolution Transmission Electronic Microscopy (TEM) bright field and Scanning Transmission Electronic Microscopy (STEM) high-angle annular dark-field (HAADF) imaging of Focused Ion Beam (FIB) produced lamellas, this strategy illuminated the sites within cytoplasm and the test where sulfur was preferentially incorporated from seawater and its association to Mg and P distribution.

2 Material and methods

2.1 Foraminiferal strain

Benthic foraminifera were grown at the free-living protist collection facility (collection group: Biological Resources of Living and Cryopreserved Cells; Collection of Unicellular Eukaryotes) at the Muséum national d'Histoire Naturelle (MNHN, Paris, France). We used the rotaliid benthic foraminifer strain For1C1 (MNHN-CEU-2016-0075, *Rosalina* sp.), initially isolated from the top layer of sediments collected off Banyuls (Mediterranean French coast) in 2006 and adapted to in vitro cell culture. The For1C1 strain can be assigned to the *Rosalina* d'Orbigny, 1826 genus because it exhibits the typical morphological characteristics described for this genus (Loeblich and Tappan, 1987). We will thus refer to it as *Rosalina* sp. Further details can be found in the Supplement and SEM views are provided in Thaler et al. (2023).

2.2 Culture in artificial seawater and ^{33}S labeling

The foraminifera were maintained through asexual reproduction in 90 mm-diameter Petri dishes in natural seawater (NSW) and fed with *Chlorogonium* sp. (strain MNHN-CEU-2016-0001), a freshwater microalga. We grew the algae under medium light intensity at 25 °C in Basal Bold medium. They were then suspended in 0.22 µm filtered pH 8.2 NSW after 3 steps of rinsing with NSW. The cultures for this study were performed similarly to the cultures described by Thaler et al. (2023). The NSW was stored in a cold room at least for a month and was then filtered through 0.22 µm filters. The pH (NBS scale) was adjusted to 8.2 through addition of NaOH and/or HCl, before use. Petri dishes were maintained at 22 °C using a Memmert IPP 110 plus incubator equipped with cold white light modules (5500 K). The light followed a 12 h day–12 h night schedule. The $^{34}S/^{32}S$ sulfur isotope ratio of the artificial seawater (ASW) sulfate has been measured at $\delta^{34}S_{ASW} = 0.1 \pm 0.2$ ‰ (Thaler et al., 2023). Though not explicitly measured, we estimate that $\delta^{33}S_{ASW} \approx 0 \pm 0.2$ ‰ because ASW most likely follows ^{33}S natural abundance.

Some individuals of the foraminiferal strain For1C1 were transferred to 0.22 µm filtered ASW prepared following Kester et al. (1967). ASW has a total salinity of $35.06\,g\,L^{-1}$, and the concentrations of the main ions are as follows (in $mmol\,L^{-1}$): Cl^- 543.9, Na^+ 467.3, SO_4^{2-} 28.2, Mg^{2+}53.1,

Ca^{2+} 9.9, K^+ 10.0, HCO_3^- 2.3, Br^- 0.8, H_3BO_3 0.4, Sr^{2+} 0.1, F^- 0.1. ASW was then left to equilibrate with the atmosphere for 2 to 3 h and the pH was adjusted to 8.2 using NaOH and HCl. Different experiments were carried out in which the specimens were cultured in enriched ^{33}S-ASW solutions containing either the natural average ocean sulfate concentration (28.16 mmol L^{-1}) or a double sulfate concentration (56.32 mmol L^{-1}). The foraminifera were left in the ASW enriched in ^{33}S for different durations (see Table 1). Specimen Fa5B was grown in ASW without labeled sulfur but fed with algae that were grown in ^{33}S enriched solution, then abundantly rinsed to avoid transferring free $^{33}SO_4$ to the growth medium of the foraminifer. Samples were then cultured for 2 to 5 d in ^{33}S-ASW seawater with a total sulfate concentration of 28.16 mmol L^{-1}, including 1.41 mmol L^{-1} of $Na^{33}SO_4$, which results in a δ^{33}S of the culture media of approximately 7030 ‰.

We selected foraminifera that were still alive at the end of the experiment, as evidenced by pseudopodial activity. Juvenile individual A1 was observed forming chambers n and n −1 in the culture medium enriched in ^{33}S (Fig. 1). Adult individuals F5(2)B, F2A2 and Fa5B were selected amongst different adult specimens after the labelling experiment and were not observed to form new chambers. Given their adult life stage, these foraminifera were less likely to produce new chambers; however this possibility cannot be completely ruled out yet.

2.3 Chemical cell fixation

Most protocols for chemically fixing foraminiferal cells involves dissolving their calcium carbonate shells using EDTA (Ethylenediaminetetraacetic acid; e.g. LeKieffre et al., 2018). Here, we present a new fixation protocol that preserves both the cytoplasm and the test. Living specimens were transferred into 2 mm diameter silicon molds. Following a protocol established for marine organisms, seawater was replaced with a Sörensen-sucrose phosphate buffer solution containing 0.1 M phosphate at pH 7.5, 0.6 M sucrose, 1 mM $CaCl_2$, 2.5 % glutaraldehyde and 1 % formaldehyde (Kopp et al., 2015). The specimens were left to soak in this solution for 24 h at room temperature then washed with three repeated baths of Milli-Q water, which was made basic to pH 9 with NH_4OH. This process removes all free ions and small molecules present in the cell (Ayache et al., 2010). Cells were then dehydrated using a graded series of ethanol solutions (50 %, 70 %, 90 % and 100 %). Finally, they were embedded in Spurr epoxy resin in four successive 1 h baths at room temperature: bath 1: 50 % resin/50 % pure ethanol; baths 2–4: 100 % resin. The resulting molds were then placed in a vacuum oven at 60 °C overnight.

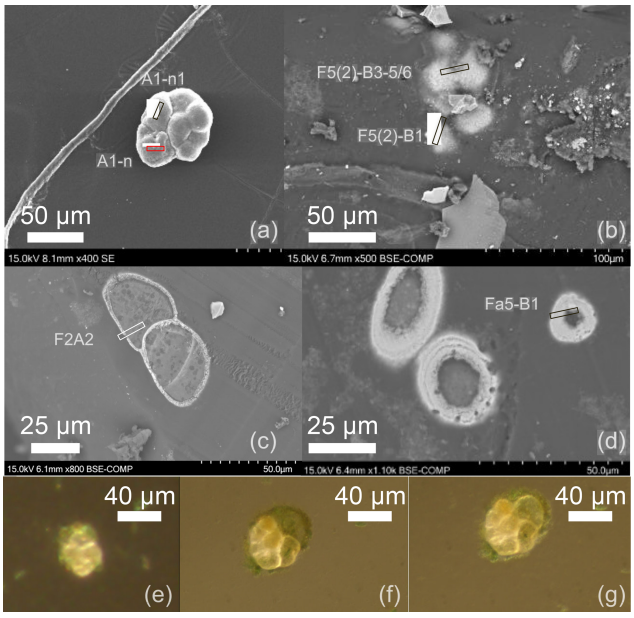


Figure 1. (a–d) Scanning electron microscope (SEM) views of the benthic foraminiferal species *Rosalina* sp. (For1C1 strain) from Banyuls, with locations of the focused ion beam (FIB) lamellas (rectangles). **(a)** Secondary electron (SE)-SEM micrograph of the specimen A1 (juvenile), not chemically fixed, and locations of the FIB lamellas in the final (n) and previous-to-last (n −1) chambers. **(b)** Backscattered electron (BSE)–SEM micrograph of the polished resin moulding of F5(2)B, showing the full chemically fixed adult specimen. The BSE detector was used to capture and select the chambers beneath the moulding surface for FIB lamella withdrawal: n −3, n −5/6 and n −1. **(c)** BSE-SEM micrograph of the chemically fixed, resin-included F2A2 adult specimen showing the location of the FIB lamella in chamber n. Here, the axial section of the specimen, at the surface of the polished moulding, provides a view of the cytoplasm inside the test, as well as the areas where the cytoplasm is still in contact with the inner part of the test. **(d)** BSE–SEM micrograph of the chemically fixed, resin-included Fa5-B adult specimen showing the chambers just emerging at the surface of the polished moulding and the location of the FIB lamella. **(e–g)** Optical microscope views of the new chambers built by individual A1 during the two days of its culture in the labeled medium: **(e)** at the start, **(f)** after 24 h, **(g)** after 48 h, end of the labelling experiment. **(e–g)** Optical microscope views of the new chambers built by individual A1 during the two days of its culture in the labeled medium: **(e)** at the start, **(f)** after 24 h, **(g)** after 48 h, end of the labelling experiment.

2.4 Focused Ion Beam sections

Focused ion beam (FIB) sections of thin lamellae were performed both on chemically fixed specimens (e.g., F5(2)B and F2A) and on non-chemically fixed specimens (e.g., A1, Fig. 1). FIB sections were produced using the FEI STRATA DB 235 FIB system at the Institut d'Electronique, Microélectronique et Nanotechnologie (IEMN, Lille, France).

We used a recently developed FIB section protocol (Aléon-Toppani et al., 2021), which enables the use of the

Table 1. Description of the different experiments/specimens analyzed by NanoSIMS.

Strain	Specimen	Sample	Sulfate (mmol L^{-1})	Duration	Fixed	chamber analyzed	Labeling
Rosalina sp. Banyuls (For1C1)	A1 (juvenile)	A1n −1	28.16	2 d	no	n −1	Sulfate
		A1n	28.16	2 d	no	n	Sulfate
	F5(2)B (adult)	F5(2)B1	56.32	5 d	yes	n −1	Sulfate
		F5(2)B3	56.32	5 d	yes	n −3 + n −5/6	Sulfate
	F2A2 (adult)	F2A2 n	28.16	2 d	yes	n	Sulfate
	Fa5B (adult)	Fa5B1	28.16	5 d	yes	n −1	Food

same FIB preparation for both NanoSIMS and Transmission Electron Microscopy (TEM) analyses. Briefly, 1 µm-thick platinum (Pt) deposit was used to shield the zones of interest. A 30 kV Ga-ion beam was used to cut 1 µm-thick lamellae perpendicular to the surface of the test, revealing its growth structure and transition with the cytoplasm. The Ga-ion beam current was chosen to minimize degradation of the FIB sections. The lamellae were then extracted and sputter damaged material was cleaned using a low-voltage, grazing-incidence Ga ion beam (5 kV). Finally, the lamellae were mounted on 1–2 µm Pt bridges, deposited in the FIB-SEM, on discoidal polished Al sample mounts that are well adapted for NanoSIMS analyses. After NanoSIMS analyses, the lamellae were recovered from the Pt bridge using the Ga beam and mounted on a TEM grid. The top surface of the FIB section was gently cleaned of NanoSIMS damage using a low-intensity Ga beam ranging from 300 pA to 1 nA. To enable TEM analysis, part of the lamellae that includes the entire growth structure of the wall and transition with the cytoplasm was thinned down to 100 nm.

2.5 NanoSIMS analyses

NanoSIMS analyses were performed using the Cameca NanoSIMS 50 at the Institut de Minéralogie, de Physique des Matériaux et de Cosmochimie (IMPMC, Paris, France) on FIB sections mounted on Al sample mounts (see section 2.3) and coated with 20 nm gold. Analyses were performed in negative secondary ion mode using a 16 keV, Cs^+ primary ion beam of 0.5 to 1 pA, ensuring a spatial resolution of 100 to 150 nm. Using entrance and aperture slits ES3 and AS2, respectively, the mass resolving power was adjusted to ensure complete separation of polyatomic interferences, including $^{32}SH^-$ and $^{33}SH^-$ at masses 33 and 34, respectively. Phosphorus and sulfur were measured as atomic ions ($^{31}P^-$, $^{32}S^-$, $^{33}S^-$, $^{34}S^-$) and nitrogen, magnesium and calcium were measured as polyatomic ions at masses 26, 40 and 56 ($^{12}C^{14}N^-$, $^{24}Mg^{16}O^-$ and $^{40}Ca^{16}O^-$, respectively) to allow measurements at the same time as P and S isotopes. Secondary ions were collected in a combined multicollection-peak jumping mode with $^{12}C^{14}N^-$, $^{31}P^-$, $^{33}S^-$, $^{24}Mg^{16}O^-$ and $^{40}Ca^{16}O^-$ measured simultaneously on electron multipliers (EM) 1 to 5, respectively, and $^{32}S^-$ and $^{34}S^-$ measured simultaneously with EM2 and EM3 using a second magnetic field value.

To achieve sputtering equilibrium and surface cleaning before each analysis, the areas were pre-sputtered for 15 min with a 10 pA beam with a raster adapted to the acquired image size. Analyses consisted in series of 10 to 15 successive image planes with raster ranging from 7×7 to 10×10 µm for images of the tests and 100 to 143 image planes with raster ranging from 10×10 to 20×20 µm for images of both tests and fixed cells. All image planes are 256×256 pixels with a dwell time of 3000 µs per pixel. The total duration of individual analyses varied from ∼ 47 min to ∼ 8 h and 6 maps were acquired on four different foraminifera specimens.

In the following, elemental results are shown as raw ratios normalized either to CaO^- or CN^-. Although the relative sensitivity factors required to determine absolute concentrations were not measured due to the lack of appropriate standards for carbonate-organic mixtures, secondary ion intensity ratios were used to account more accurately for variations of these instrumental mass biases, thus allowing the determination and study of relative variations of the intensities of Mg and S in the carbonate matrix. Secondary ion intensities are reported in total number of counts (cts) over the course of an analysis.

$^{34}S/^{32}S$ and $^{33}S/^{32}S$ ratios are presented as δ values uncorrected for instrumental mass fractionation (IMF), again due to the lack of appropriate standard for its proper determination in carbonate-organic mixture. The $^{34}S/^{32}S$ ratio was used as an internal reference for each acquisition to ensure that this IMF remained negligible within uncertainty and to monitor the stability and reproducibility over the duration of the analytical session. S isotopic ratios are reported in ‰, where $\delta^{3x}S = (^{3x}S/^{32}S)_{sample}/(^{3x}S/^{32}S)_{V\text{-}CDT} - 1$. V-CDT is the international Vienna Canyon Diablo Troilite standard. Because the main source of uncertainty is by far counting statistics within regions of interest (ROI) of variable sizes extracted from the images by image processing, reported errors correspond to counting statistics and are controlled by secondary ion intensities of the minor isotopes.

Images were corrected for detector dead time (44 ns) and lateral drift during analysis. Data from ROIs within images and intensity profiles were extracted from bulk images with summed individual cycle planes using the LIMAGE software (© L. Nittler).

2.6 Electron Microscope analyses

Scanning electron microscope (SEM) images of foraminifera in secondary electron (SE) and backscattered electron (BSE) modes have been taken at the Electron Microscopy Platform (PtME) of the Muséum national d'Histoire Naturelle (MNHN, Paris, France) using a Hitachi SU3500 environmental SEM (Fig. 1). High resolution Transmission Electron Microscope (TEM) bright field and high-angle annular dark-field (HAADF) Scanning Transmission Electron Microscope (STEM) imaging of FIB lamellas were performed on a spherical aberration-corrected JEOL ARM 200 F microscope operating with a cold Field-emission Electron Gun (FEG) at 200 kV at the Advanced Electron Microscopy Platform, Materials and Quantum Phenomena Laboratory (MPQ, Paris, France). For the HAADF-STEM imaging the length of the camera was of 80 mm. The TEM views were produced on the exact same section on which NanoSIMS observations were performed, following a recently developed protocol (Aléon-Toppani et al., 2021). TEM views provided here are obtained with a 5° tilt. Additional views with −5 and 0° tilts are available as Supplement figure (Fig. S1).

3 Results

3.1 Electron Microscope observations of the test wall microstructure

Both bright field TEM and HAADF-STEM observations reveal the multi-layer growth microstructure of the chamber wall of a *Rosalina* sp. specimen remarkably well in the FIB lamella F5(2)B1, which was cut perpendicular to the surface of chamber $n-1$ (Fig. 2). The dark color of the layers in the bright-field TEM image (Fig. 2a) suggests that they are crystalline because they are in diffraction position and correspond to the inner (ICL) and outer (OCL) calcitic layers. Furthermore, the orientation of the darker and lighter grey zones changes preferentially between the two outer calcitic layers. Notably, there is a lateral alternance of white, light grey and dark grey oblique zones, especially in the main calcitic layer of the chamber (OCL_{n-1}). We count two additional OCL, one that we identify as OCL_n and another, much thinner one. We interpret it as being associated to the onset of the building of a new chamber, possibly interrupted as the foraminifera was transferred to the labeled medium. This OCL will be labeled as OCL_{n+1}. The TEM bright field oblique white zones correspond to the darkest oblique zone in the STEM images and reveal a non-crystalline, less dense nature similar to that of the organic layers (IOL, POS, OOL).

The white zones that draw irregular lines in Fig. 2a are interpreted as non-crystalline structures for three reasons. First, the portion of the FIB lamella analyzed by TEM is homogeneous in thickness, thus changes in brightness cannot be explained by a change in thickness of the sample. Second, brighter areas in bright field TEM views are explained by less dense and/or less crystalline structures. Third, changing the tilt of the section does not modify the brightness of those zones (Fig. S1), which is best interpreted as amorphous/non crystalline structures. In contrast, the dark zones show that the material is crystalline, with different orientations because the level of darkness changes with a modification of the tilt (Fig. S1). HAADF imaging supplements the information provided by TEM. The level of darkness in the image of Fig. 2b can indicate the average density and chemical composition of the structures, with darker areas indicating "lighter", less dense material and lighter areas indicating denser material with a heavier chemical composition. Thus, the four almost continuous layers that appear white in the TEM bright-field view (Fig. 2a) and black in the HAADF-STEM view (Fig. 2b) are characterized by non-crystalline, less dense and composed out of lighter elements and likely correspond to the IOL, POS and OOL of the chamber $n-1$, as well as the OOL_n and OOL_{n+1}. The POS is found alongside coarse, block-like amorphous/organic phases (see Fig. 2c and d). Overall, these images clearly show the addition of a new OCL_n, and the inner wall IOL_{n-1}–ICL_{n-1}–POS–OCL_{n-1}–OOL_{n-1}–OCL_n–OOL_n–OCL_{n+1}–OOL_{n+1} microstructure (Fig. 2a, b).

Furthermore, the shades of grey within the OCLs (darker or lighter) in bright-field TEM views mostly reflects crystal orientation within the polycrystalline structure of the test. In the STEM image (Fig. 2b), the calcitic layers appear homogeneous, indicating homogeneous density, which could support the interpretation of the bright field TEM shades as reflecting crystal orientation. At high resolution, the outer calcitic layers reveal a nanogranular structure. This structure appears darker in the STEM image (Fig. 2j) and brighter in the TEM images (Fig. 2h and i) than the grey background. This suggests that these "nanogranules" are less dense, lighter and less crystalline than the surrounding calcite.

3.2 Distribution of P, Mg and S in the test

NanoSIMS maps reveal the distribution of natural and isotopically labeled sulfur, enabling us to compare the distribution of sulfur to that of organic matter, calcium carbonate, and Mg/Ca banding across the microstructure of the test's wall growth. Using Ca ($^{40}Ca^{16}O$) and CN ($^{12}C^{14}N$) maps, we are first able to distinguish the test mainly composed by calcium carbonate, thus, by definition, rich in Ca, from the cellular organic matter rich in CN (Fig. 3, Supplement Figs. S2 and S3). In this regard, the FIB lamella across foraminifer F5(2)B reveals the most distinct S/Ca, P/Ca and Mg/Ca distributions that follow the microstructure of the test (Figs. 3,

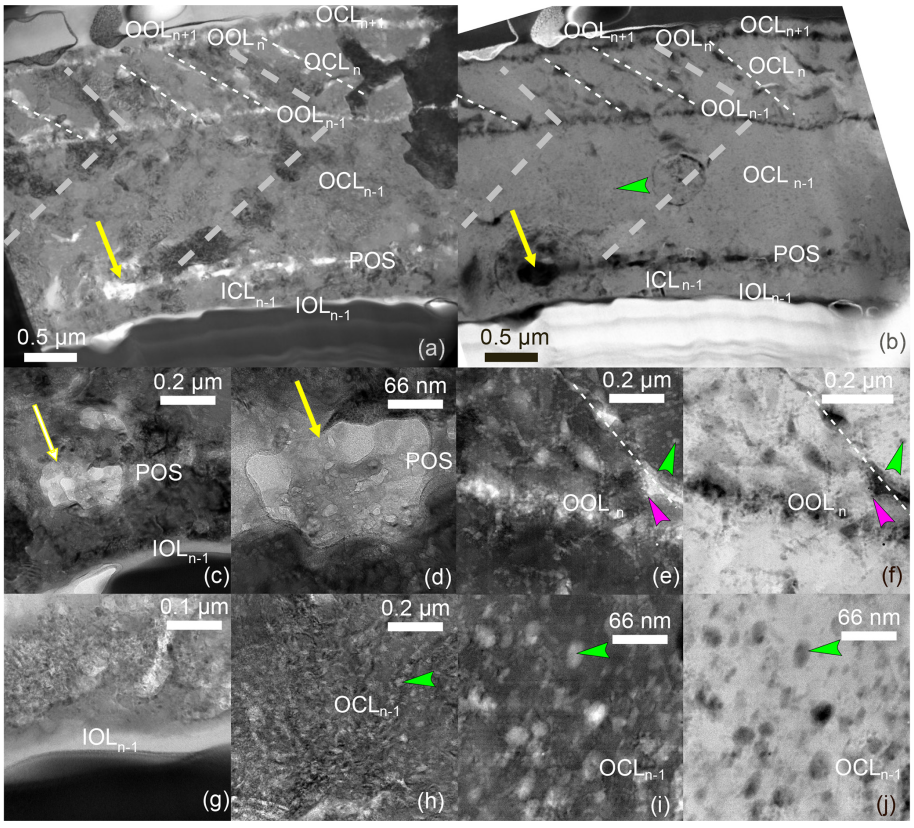


Figure 2. TEM bright field **(a, c, d, e, g–i)** and HAADF-STEM **(b, f, j)** images from the FIB of foraminifer F5(2)B (chamber n −1, sample F5(2)B1) taken after NanoSIMS analysis. **(a)** The global view of the FIB section shows amorphous areas (white) and crystallized zones (dark grey to darker grey) within the test. **(b)** In HAADF-STEM view, they correspond to less (dark) and more (grey) dense areas, respectively, with lighter (dark) and heavier (grey) chemical composition. Oblique dotted lines are additional structures found within the OCL_n. The very thin most external OCL is the final chamber that the foraminifer started building right before it was transferred (OCL_{n+1}) with the most external OOL (OOL_{n+1}), that is only partially preserved along the test. The white dotted lines likely correspond to amorphous-less dense oblique structures that are comparable to the different OLs, while the grey dotted line correspond to a TEM bright field structure that is not found within the HAADF image. The dense material at the base of the test **(b)** corresponds to the Pt deposited during the preparation of the FIB. In TEM bright field images, the IOL_{n-1}, POS, $OOL_{n-1}$and OOL_n are recognizable by white discontinuous layers that appear black in HAADF-STEM images. **(c, d)** Close up view of the POS, with a focus on the area rich in white amorphous blobs, indicated by a yellow arrow, **(e, f)** detail of OOL_n; showing the organic-less dense OOL itself, as well as the base of one of the oblique structures from within OCL_{n-1} **(g)** close-up view of the cell-test transition highlighting the IOL; **(h–j)** detail of the nanogranular structure in the calcitic layers, here OCL_{n-1}. Green arrowheads point towards an example of nanograin in the calcitic structure at different scales, fuchsia arrowheads point towards similar nanograins on the edge of the organic lining. This sample is the same as in Figs. 3 to 6.

4). A pronounced banding is observed, characterized by thin bands with high Mg/Ca, P/Ca and S/Ca ratios in the inner and outer parts of the test, separated by a broader band characterized by lower ratios. The FIB section is surrounded by two thick layers of platinum deposits, one of them constituting the dark (Fig. 2a) or white (Fig; 2b) layered area at the base of the FIB. The layers can be seen in the SEM view (Fig. 3f). The FIB was performed on chamber n −1, whose cytoplasmic content could have retracted during the fixation process, creating a gap. The cutting process during FIB extraction likely pulverized some of the cellular material attached to the test, which was then redeposited in the gap between the wall and the cytoplasmic material, where it mixed with platinum. These layers are thus an artefact of the FIB lamella preparation process and are excluded from further interpretation.

Cross plots of element distribution within the test allow to better understand this repartition (Fig. 4, Table S1). We observe three trends in S/CaO vs. CN/CaO distribution (Fig. 4a). Trend A (yellow circles, Fig. 4) corresponds to the strongest P, S and Mg enrichments in relation to CN. While S/CaO and MgO/CaO values remain higher than 1 or 0.15 cts cts^{-1}, respectively, P/CaO ratios go all the way down to zero, suggesting that, unlike P, S and Mg have a background occurrence. Points defining trend A are in OCL_{n-1} and OCL_n, including OOL_{n-1} and OOL_n. Trend

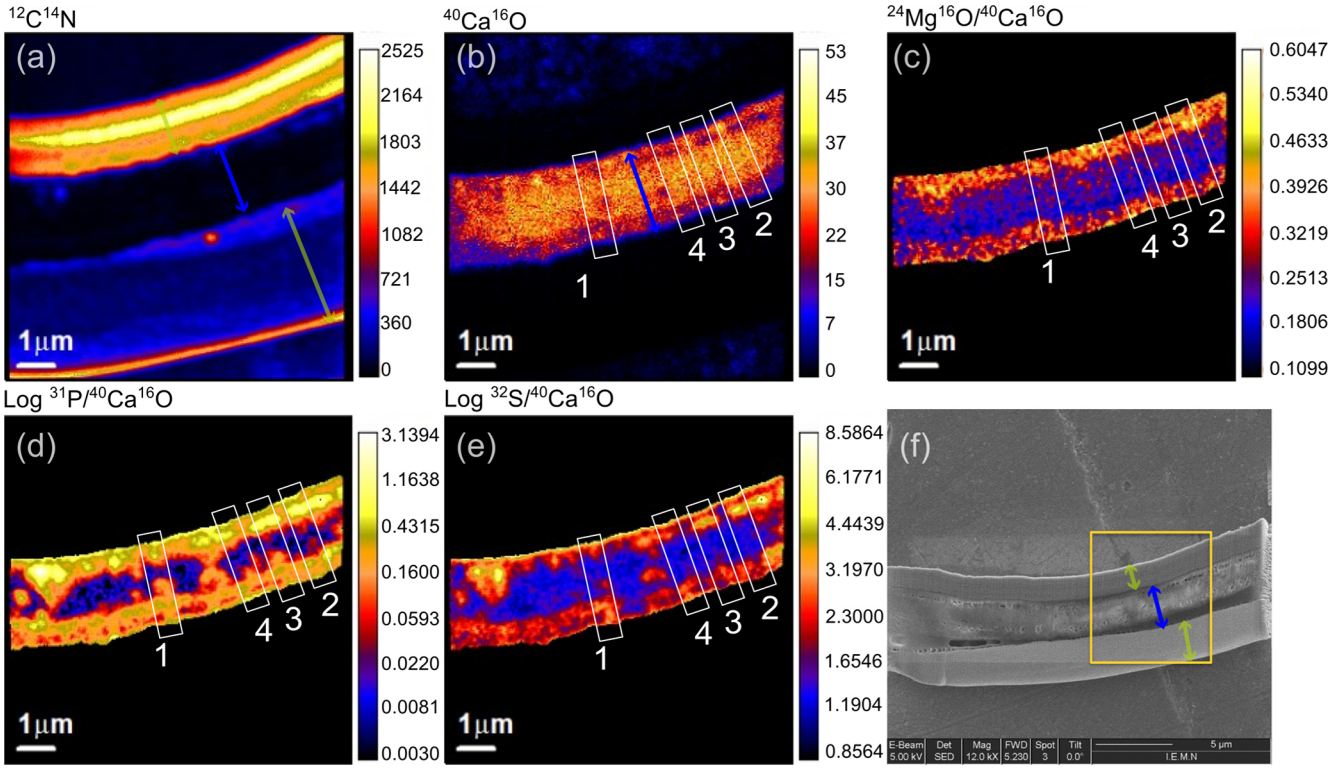


Figure 3. $^{12}C^{14}N$ **(a)**, $^{40}Ca^{16}O$ **(b)**, $^{24}Mg^{16}O/^{40}Ca^{16}O$ **(c)**, $^{32}S/^{40}Ca^{16}O$ **(d)** and $^{31}P/^{40}Ca^{16}O$ **(e)** maps across the FIB section **(f)** chamber n − 1 of foraminifer F5(2)B (sample F5(2)B1), cultured in doubled sulfate concentration seawater. Open white rectangles indicate the location of the profiles from Fig. 4. The orange square in **(f)** indicates the location of the superposition between the NanoSIMS mapping and the TEM-STEM views (Fig. 5). MgO/CaO, S/CaO and P/CaO are represented only for the test. A mask was applied to avoid divergence due to the low CaO emission in the cell. Note that for P/CaO and S/CaO, the color scale is represented for the log of these ratios. Green arrows = platinum deposits; blue arrow = test.

B (orange circles, Fig. 4) is even more P-and S-enriched compared to Trend A. However, the highest values are not systematically reached in all profiles, and trend B is most clearly visible in profiles 2 and 3, compared to profiles 1 and 4 (Figs. 4j–l; S6; S7). Trend B corresponds to the enrichments of P, S and Mg across the POS. Finally, trend C (blue circles, Fig. 4) suggests an N-rich component where P, S and Mg remain at moderate levels. CN/CaO ratios become extremely high. Trend C occurs only on the edges of the test (see Figs. S6; S7 and Table S1) and could be either characteristic of IOL_{n-1} and OCL_{n+1} or due to an artificial decrease of the CaO signal and increase of the CN signal as the end of the test is reached and the beam overlaps the CN-rich deposits. The non-zero beam size leads to an averaging across the major matrix change from calcite to cytoplasm, where S, P, Mg/Ca and Ca/CN values appear high (e.g. Figs. 8, S6). As a result, in the following, we will consider only measurements with CN/CaO values below 40, P/CaO below 1 and S/CaO below 5. Values above those thresholds are found only on the edge of the tests with the extension of trend C.

Finally, when normalized to CN and not to CaO, the covariations of S and P become obscure, and appear even anti-correlated within the points that follow trend A, suggesting that OM is not the common carrier of the two elements at least in this trend (Fig. 4i).

Mg/CaO, S/CaO and P/CaO distributions across the growth structure of the wall of chamber n − 1 of *Rosalina* sp. F5(2)B share common trends (Figs. 4, 5. Table 2). It should be noted first that structures smaller than the beam size (100–150 µm) cannot be distinguished and that values close to the edge are affected by the averaging across the beam surface, as mentioned previously. Overall, the outer calcitic layer deposited during the formation of the chamber selected for the FIB (OCL_{n-1}) has the lowest concentration in all three elements. Contrastingly, all three ratios are higher in both ICL_{n-1} and the outer calcitic layer deposited while the following chamber was formed by the foraminifer (OCL_n). NanoSIMS resolution does not allow us to investigate the composition of OCL_{n+1} whose width is about the same as the beam size.

Phosphorus reveals four enriched bands. Both P/CaO and P/CN ratios indicate the same pattern and allows to track the POS zone, as well as OCL_n, both enriched in this element. Both edges however, including the IOL and the OOL_{n+1}, ap-

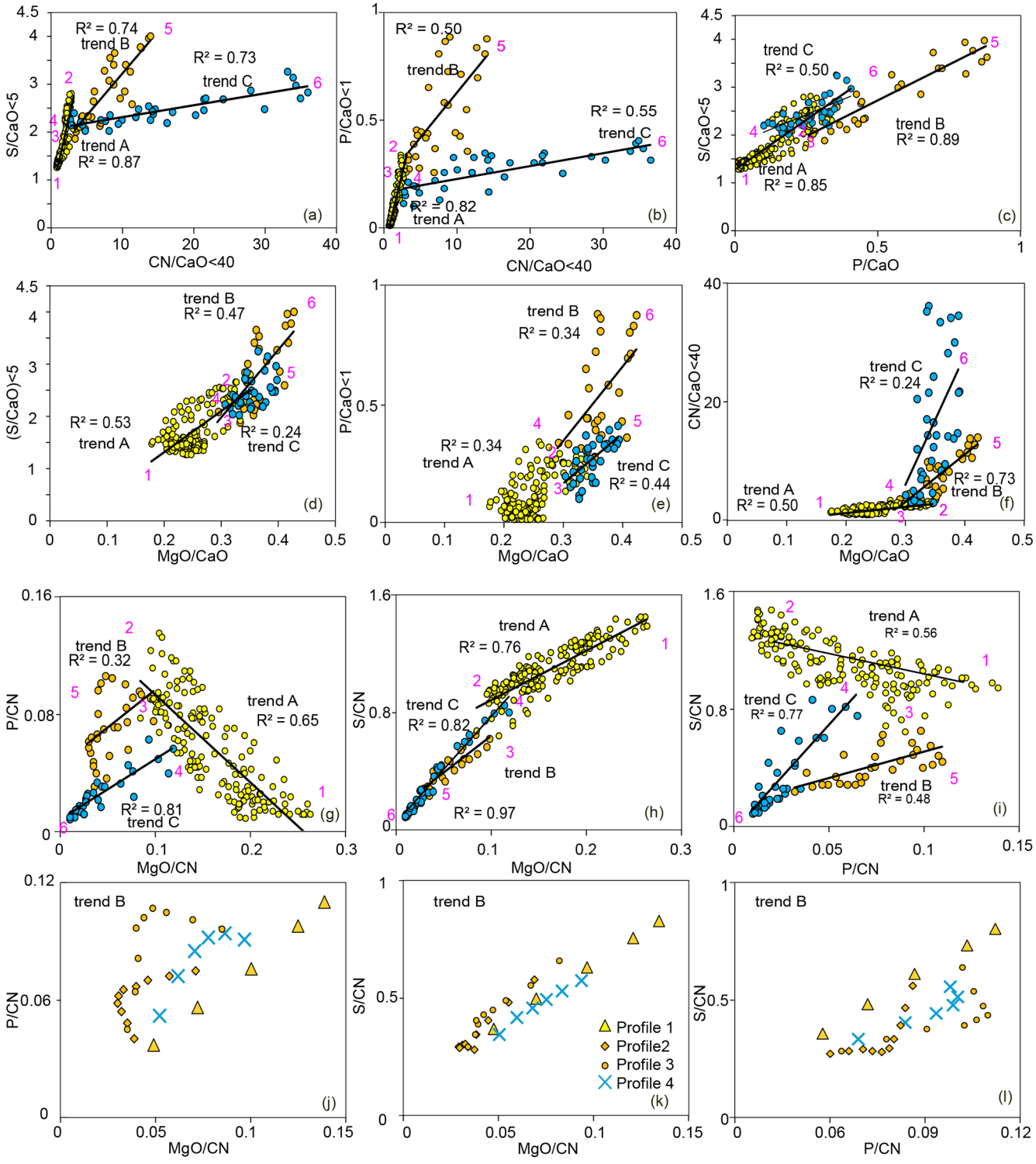


Figure 4. Cross plots of elemental distribution across the test combining 4 profiles across the F5(2)B1 section, with three indicative trends A, B and C. Purple numbers indicate the transition between the trends. Only values corresponding to CN/CaO < 40 cts cts^{-1} are chosen as values above this threshold correspond to the extension of trend C, likely affected by edge effects. Ratios are given in cts cts^{-1} and provide the relative distribution of elements but not absolute values. Location and full datasets of the profiles are shown in Figs. 3 and S6, respectively. **(a–i)** The color code is based on those trends (see Fig. S7 and Table S1) Black lines are linear regression with the R^2 coefficient indicated close to them. **(a–f)** elements are normalized to CaO. **(g–l)** elements are normalized to CN. **(j–l)** points from trend B are individualized by profiles to show the different individual trends and their different P-enrichment on top of Mg, S and P shared enrichments.

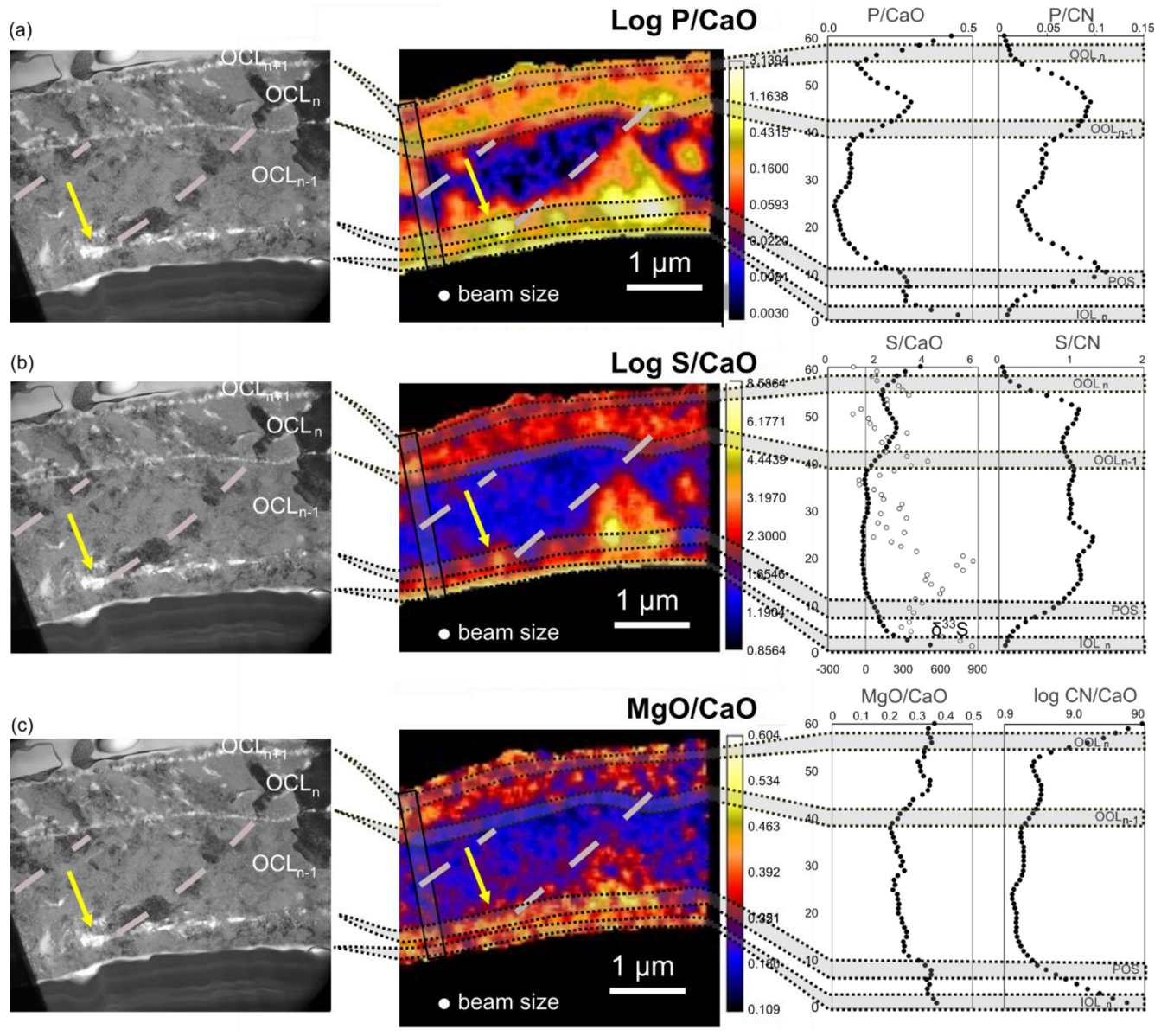


Figure 5. Combination of bright field TEM images from Fig. 2 with elemental maps and profiles showing the distribution of elements and elemental ratios across the wall of the chamber n −1 of foraminifer F5(2)B. The yellow arrow points to the same non crystalline blob as in Fig. 2. The rectangle with solid black lines indicates the location of profile 1 (same profile 1 as in Figs. S5 and S6, profile location shown Fig. 3), used to trace P/CaO, P/CN, S/CaO, S/CN, MgO/CaO and CN/CaO. The grey dotted lines indicate successions of darker TEM bright-field zones that make the transition from P, S and Mg-rich areas to P, S and Mg-poor areas.

pear excessively high in P/CaO and low in P/CN, which could be due to edge effect related to the beam size. As marked by the yellow arrows in Figs. 2 and 5, within the POS, and all the way inside the wall, the less crystalline areas are associated with the highest concentrations in phosphorus. The dashed lines in Fig. 5 reveal three darker areas that mark the limit of a P-rich zone that corresponds to some of the blobs visible in the POS, similar to the one pointed by the yellow arrow (Figs. 2, 5). These areas are highly enriched in P and delineate zones that extend beyond the POS. These darker areas are not discernible in the HAADF-STEM view, suggesting that they are of identical density to the surrounding less dark areas. We interpret the level of gray as a possible difference of crystal orientation within the OCL.

Co-bandings of sulfur and magnesium, as well as of S and P (or other elements assumed to reflect the presence of organic matter, such as N), have been documented in foraminifera (Paris et al., 2014b; Glock et al., 2019; van Dijk et al., 2019b; Geerken et al., 2019; Lemelle et al., 2020). However, in detail, the relationships between the bands are

Table 2. Individual correlations (R^2 value) within each trend identified in Fig. 4.

Ratios to Ca	P vs Mg	P vs CN	S vs Mg	S vs CN	CN vs. Mg	S vs P
trend A	0.34	0.82	0.53	0.87	0.50	0.85
trend B	0.34	0.50	0.47	0.74	0.73	0.89
trend B prof. 1	0.91	0.07	0.90	0.83	0.21	0.38
trend B prof. 2	0.71	0.74	0.80	0.90	0.9	0.93
trend B prof. 3	0.79	0.30	0.90	0.57	0.68	0.91
trend B prof. 4	0.90	0.55	0.60	0.86	0.75	0.95
trend C	0.44	0.56	0.23	0.73	0.24	0.50
trend A + C	0.58	0.44	0.67	0.43	0.50	0.85

variable. S-bands and P-bands tend to be sharper than Mg-bands in profiles across tests of the benthic foraminifer *Amphistegina lessonii* and *Ammonia tepida* (Geerken et al., 2019), while S-bands appear broader than Mg-bands in the planktic foraminifer *Orbulina universa* (Paris et al., 2014a). In the last chamber of the planktic foraminifer *Globorotalia menardii*, the S- and Mg-bands are very well correlated and comparable in width, though S follows a pattern that is hybrid between P and Mg, with enrichments of all three elements in the POS (Lemelle et al., 2020). In the planktonic species *Uvigerina striata*, cleaning removes a diffuse and patchy organic matter from the test (Glock et al., 2019). Interestingly, despite the absence of cleaning, we do not observe such a patchy distribution in the samples. Here, S also displays a behavior that is hybrid between P and Mg distributions, with the same general organization. P and S follow a sharp band in the POS, while Mg is broader. Contrastingly, only P follows such a sharp pattern between the OOLs, while both Mg and S peaks tend to be more extended into the rest of the test. Here, ^{33}S enrichment is observed only in OCL_{n-1}, near the POS.

Finally, the coincidence between the different structures of the test and the composition is revealed through the superposition of TEM and NanoSIMS images. They reveal that the different OOL are associated to transition between chemical compositions more than they are associated to local maxima or minima. Overall, the comparison between the different results underline that NanoSIMS observations are more sensitive to chemical changes than to structures (as exemplified by OOLs or P/CaO maxima not associated with any change in density or diffraction in HAADF-STEM and bright-field TEM views, Fig. 5).

3.3 Element distribution in the cytoplasm

Cytoplasm that remains attached to the test (see for instance Figs. S4 and S5) displays heterogeneities in the distribution of elements. NanoSIMS images of the FIB lamella of the chamber (n −3) of the specimen F5(2)B and of the last chamber (n) of the specimen F2A (Fig. 7) reveal a notable degree of heterogeneity in the distribution of Ca, P, Mg and S in the cytoplasm. The cytoplasm contains areas that are strongly enriched in sulfur (^{33}S) (white arrows, Fig. 7d–e, j–i), which seems to correlate with relatively high sulfur (^{32}S) values in the final chamber (n) of the F2A specimen (Fig. 7k). Some large vesicles appear "empty", because the original liquid or soluble components inside the vesicles were most likely removed during the chemical fixation and the embedding in the epoxy resin. Some other large vesicles contain granular structures that are enriched in P, Ca and Mg (Fig. 7b, c, f green arrow) or in Ca and ^{33}S (Fig. 7i, j red arrow). Other smaller vesicle-like structures are rich in Mg, P and Ca (Fig. 7b, c and f, green arrow), or contain P, Ca, Mg and S (Fig. 7h, k, l, magenta arrows). The 2–3 µm Ca-rich vesicle near the IOL of the last chamber of the FA2A specimen (Fig. 7g–k), though not enriched in sulfur (Fig. 7k), contains ^{33}S (Fig. 7j). Unlike the previously described structures, it does not contain phosphorus or Mg. Another vesicle right below this vesicle, of the same size, though devoid of calcium, also shows heterogeneous ^{33}S distribution.

The CN, P and S maps enable us to trace a continuous layer, likely the inner organic layer (IOL), at the transition between the interior of the test and the endoplasm (the cytoplasm inside the cell) (Fig. 7a, b, e, g, h, k). However, the composition contrast at the test-cytoplasm interface needs to be considered with the greatest care because of the obvious matrix change. Throughout the cytoplasm, vesicles-like structures of different sizes are present. The inside of these vesicles can be grouped in three categories: seemingly "empty" (most likely because of the chemical fixation), enriched in P, Ca, Mg and moderately in S (green arrows in Fig. 7) or rich in Ca only, though unevenly (red arrow in Fig. 7).

Images taken for specimen Fa5B (Fig. 8) reveal the path of sulfur from food through the trajectory of ^{33}S ingested with algae (reaching ratios of $\sim 5\,\%$) along with unlabeled sulfur with natural δ^{33}S ratios within error (lower than $\sim 100\,‰$). The images reveal that in that case, labeled sulfur occurs as small grains within the cytoplasm, often enriched in Mg (grey arrowheads), but not systematically (blue arrowheads) and not highly enriched in Ca. This labeled sulfur is not found in the test, which did not grow during the culture experiment.

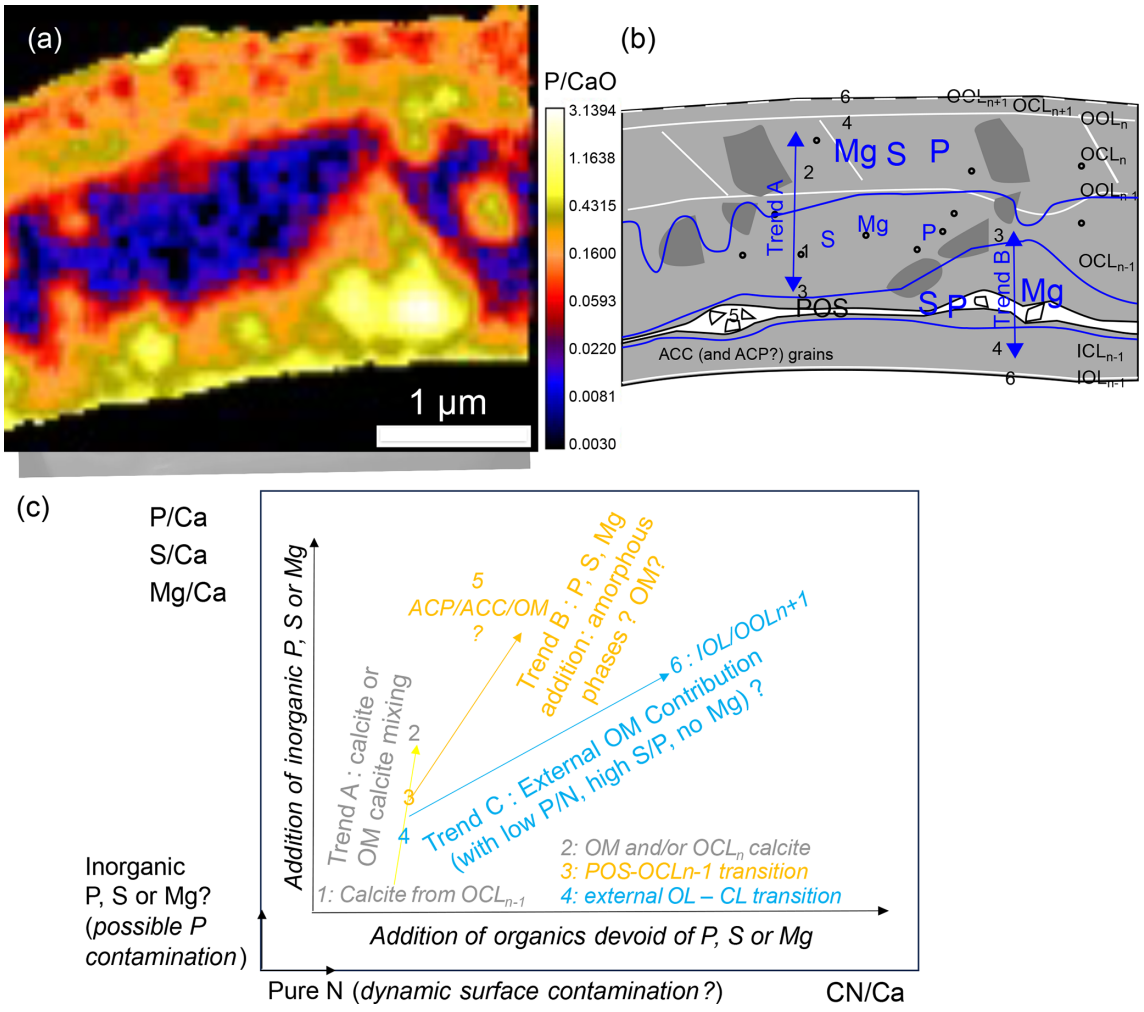


Figure 6. Superposition of the TEM view and the P/CaO map **(a)** and synthetic summary of the observations **(b)**. In blue, information from the NanoSIMS analyses. The size of the letters reflects the relative abundance of the elements; trends A and B are from Fig. 4. White and gray reflect the TEM observations. The white lines are the POS associated with amorphous blobs as well as the OLs and the levels of gray from the CLs, reflecting the change of orientation from one side and the other of OOL_{n-1}. The numbers represent the different endmembers from Fig. 5. They are explicated in panel **(c)**. **(c)** schematic view of the different trends (letters), drawn as mixing lines between two endmembers (numbers): schematically, A = 1 + 2, B = 3 + 5, C = 4 + 6.

3.4 Sulfur isotope ratio values and incorporation of ^{33}S in the test

We produced maps of ^{32}S, ^{33}S and ^{34}S and analyzed isotope ratios (Fig. 9). Measured uncorrected $\delta^{34}S$ values range from to -13 ± 11 ‰ (1SD) to -1 ± 14 ‰ in calcite, while they range from -9 ± 8 ‰ to 13 ± 11 ‰ in organic matter, in the range of natural abundances. The $\delta^{34}S$ values we measured for sulfur present in the test are very close to that of the artificial seawater in which the foraminifera grew ($\delta^{34}S_{ASW} = 0.1$ ‰, Thaler et al., 2023). Small differences may arise, but the analytical reproducibility (roughly ±8 ‰) and the absence of suitable reference materials do not allow us to investigate them. This confirms nonetheless that the instrumental mass fractionation (IMF) is likely small, within uncertainties; and that the corresponding correction can be neglected in the examination of $\delta^{33}S$ values that change widely because of the artificially increased amount of ^{33}S. The similar values between organic matter and calcite also indicates that matrix-related instrumental effects can be neglected in the following in regard to the observed variations and uncertainties. Clear variations of $\delta^{33}S$ values are observed, from 174 ± 28 to 5556 ± 68 ‰ in the test and from 1827 ± 44 to 3072 ± 36 ‰ in organic matter (Table 3). The values cannot be explained by a fractionation of such magnitude, which furthermore should have affected the $^{34}S/^{32}S$ ratios even more strongly. Whereas the values of $\delta^{34}S$ are similar in organic matter and calcite within errors, $\delta^{33}S$ values differ between these two components, with no systematic tendency. Instead, the observed values reflect

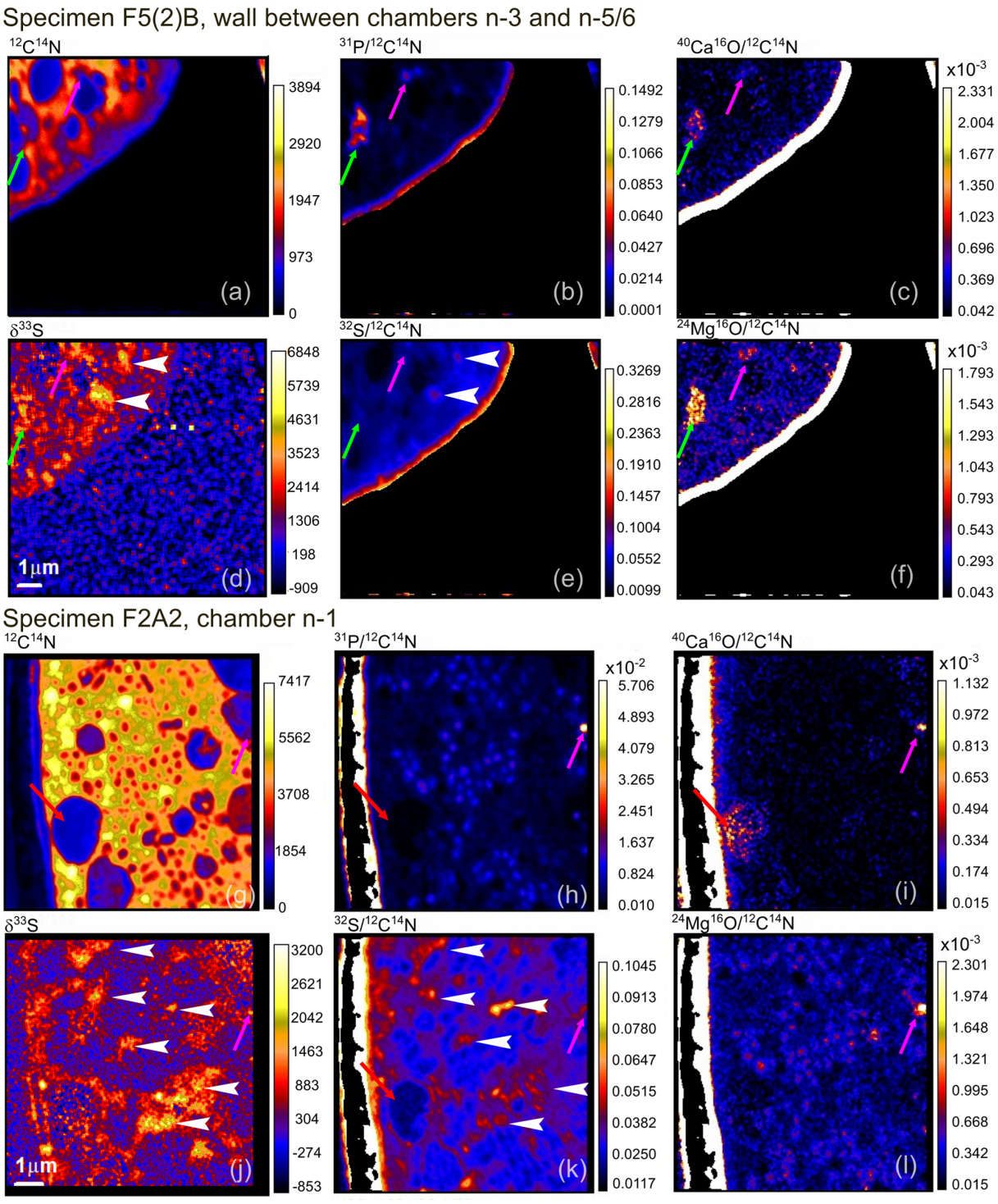


Figure 7. $^{14}C^{12}N$, $^{31}P/^{14}C^{12}N$, $^{40}Ca^{16}O/^{14}C^{12}N$, $\delta^{33}S$ (‰), $^{32}S/^{14}C^{12}N$ and $^{24}Mg^{16}O/^{14}C^{12}N$ maps in the cytoplasm and test of chambers n −3 from foraminifer F5(2)B **(a–f)** and chamber n −1 from foraminifer F2A2 **(g–l)**. A mask has been applied over the tests. The green arrow points to irregular P, Ca, Mg-rich 2 µm structures also enriched in ^{33}S, magenta arrows to ∼0.5 µm grains rich in P, Mg, Ca and S, with ^{33}S enrichment. White arrowheads point to small (0.5–1 µm) structures enriched in sulfur and ^{33}S and grey arrowheads follow a succession of Mg-rich grains. Inside the cell of F2A2, P-rich and S-poor grains can be observed, while S is enriched in between those grains. The red arrow points to a ∼3 µm vesicle with Ca rich grains on the side close to test and ^{33}S rich on the other side. Position of the images with respect to the complete specimen are given in Fig. 1.

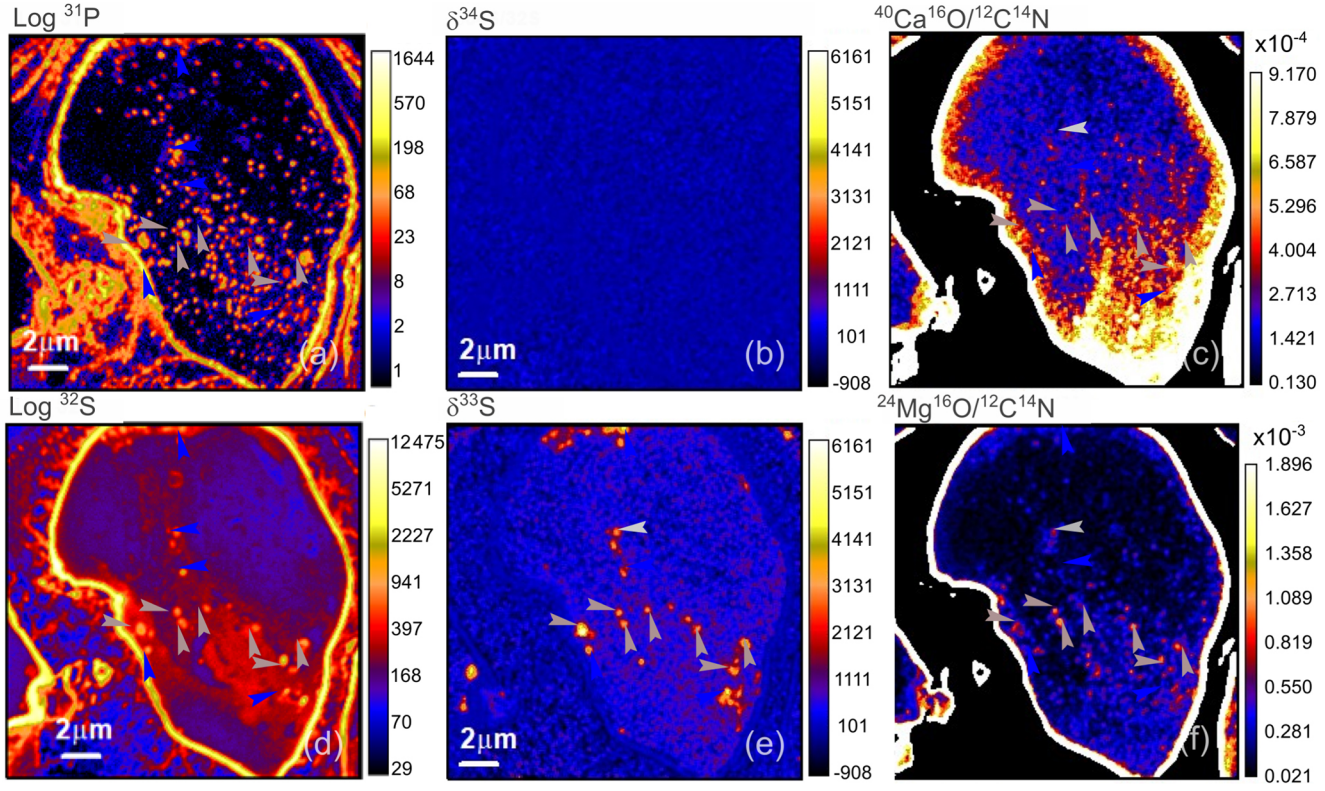


Figure 8. Log ^{31}P, δ^{34}S (‰) ^{40}Ca^{16}O/^{14}C^{12}N, Log^{32}S, δ^{33}S (‰) and ^{24}Mg^{16}O/^{14}C^{12}N maps in the cytoplasm and test of chamber n −1 from foraminifer Fa5B1 **(a–f)**. A mask has been applied over the test in maps **(c)** and **(f)**. Grey arrowhead point to P, S, ^{33}S and Mg rich granules while blue arrowhead point to S and ^{33}S rich only granules. For a direct comparison, a similar color scale has been applied to δ^{33}S and δ^{34}S images.

a mixing between isotopically labeled (∼ 7030 ‰) and non-labeled (∼ 0 ‰) sulfur. We also note that the higher the δ^{33}S is in calcite, the higher it is also in organic matter.

4 Discussion

4.1 Control of sulfur occurrence at the sites of biocalcification

Interpretation of δ^{33}S of the test depends primarily on the amount of calcite grown in labeled seawater. In most experiments, chambers formed before the foraminifera was transferred to the labeled seawater and the tests show little to virtually no ^{33}S enrichment (e.g., Figs. 7d, j or 9h). Labeled sulfur, thus initially introduced as sulfate, can be found within the test, as well as within the organic matter of the last two chambers of specimen A1, which grew in labeled seawater (Fig. 9b, e, Table 3). The high values of δ^{33}S (∼ 5300 ‰ in average) in both chambers suggests that ≈ 3/4 of the sulfur in the test comes from seawater sulfate, which was taken up during the precipitation of the test from the calcification fluid derived from labeled ^{33}S seawater. Though some of the remaining sulfur is likely to be unlabeled organic sulfur, this number is a low estimate of the sulfur from seawater sulfate present in the test because chamber n −1 is slightly less enriched (δ^{33}S ≈ 5190 ‰) than the last chamber (δ^{33}S ≈ 5560 ‰). The difference between the two chambers could suggest that more labeled sulfate is incorporated in the last chamber, after the individual spent more time in labeled seawater. Thus, part of the incorporated sulfur could have been previously stored in the cell, and/or comes from the unlabeled food. However, the homogeneity of δ^{33}S values, that reveal no correlation with organic banding in the test, suggests that less than 1/4 of the sulfur is ultimately sourced from food. We have no observational evidence that F5(2)B or F2A2 grew chambers in the labeled medium, and the NanoSIMS images of the wall of the penultimate chamber of F5(2)B (Fig. 9h) shows no massive ^{33}S enrichment such as the one found in A1, which supports the idea that the chambers we observe here were grown in the unlabeled medium. Yet, the organic matter on the inner side of the test of these cells contains ^{33}S, more than the test (Table 3). However, as previously explained, the cytoplasmic remains have been significantly altered during the FIB process and to the very least homogenized. Thus, the sulfur data from Fig. 9 must be considered extremely cautiously for the or-

Table 3. Summary of the average measured uncorrected δ^{34}S and aδ^{33}S values of the test and organic matter (OM) of the samples analyzed only for FIB section of tests only.

FIB	image	δ^{34}S test	δ^{34}S OM	δ^{33}S test	δ^{33}S OM
A1(n−1)	20	-9 ± 6	-9 ± 6	5193 ± 70	2478 ± 23
A1(n)	21	-11 ± 11	-9 ± 8	5556 ± 68	3072 ± 36
F5(2)B1	23	-13 ± 12	13 ± 11	174 ± 28	1827 ± 44

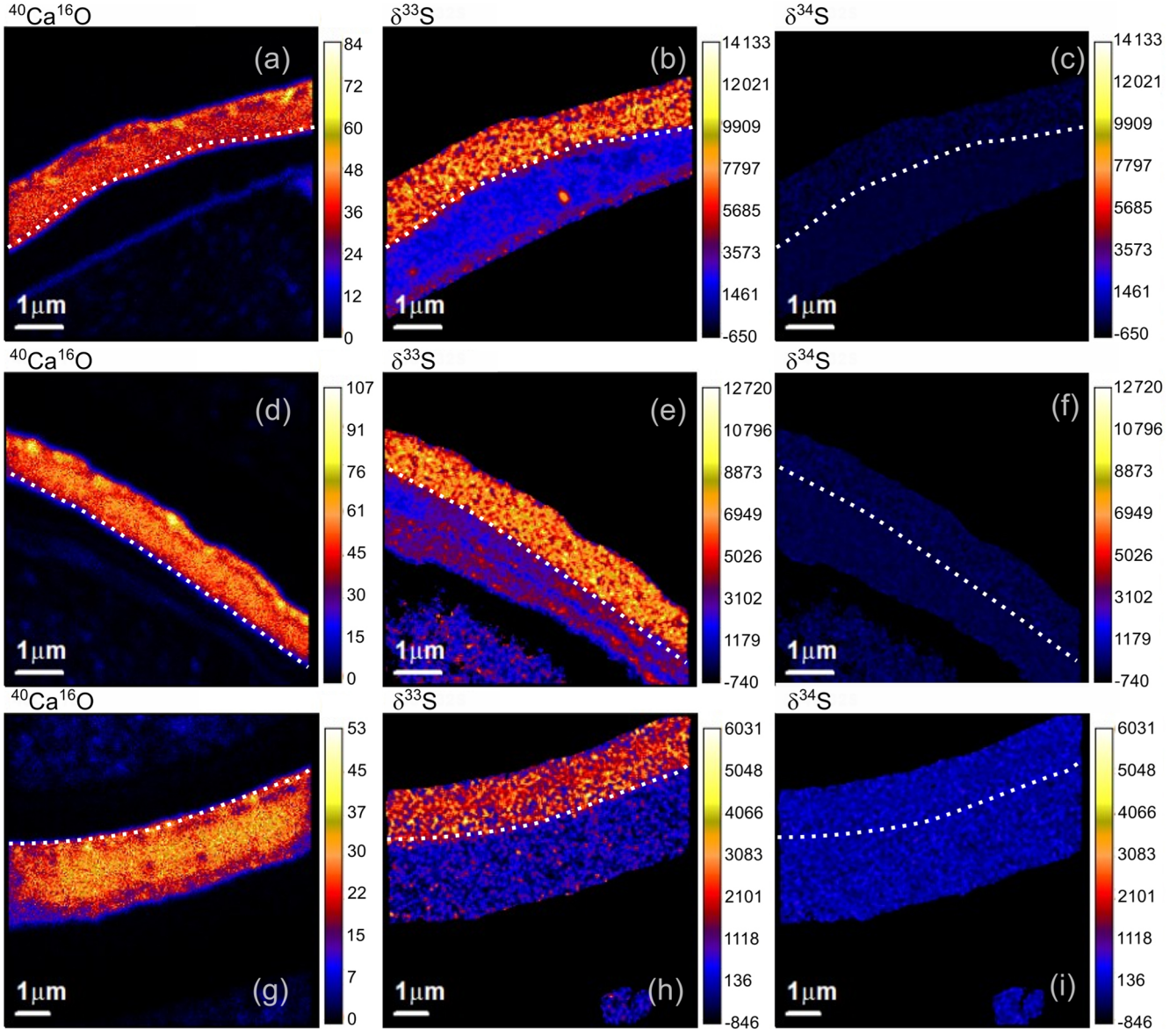


Figure 9. CaO (cts), δ^{33}S (‰) and δ^{34}S (‰) maps across the walls of foraminifer A1 chamber n−1 **(a–c)** and n **(d–f)** and the wall of chamber n−1 of foraminifer F5(2)B **(g–i)**. The dotted lines represent the limit between the test and the organic matter. Note that similar color scales have been applied to δ^{33}S and δ^{34}S images for direct comparison.

ganic matter. Modest ^{33}S enrichments can be found locally within the test of specimen F5(2)B (Figs. 5b, S7), sometimes along OOL_{n-1} and OOL_n, sometimes close to the POS, and within the cytoplasm of other samples (Figs. 7d,j; 8e). Seawater sulfate is thus somehow added by the cell during the duration of the experiment in previously formed chambers, both in the cytoplasm and the test.

Our observations shed new light on the tight control of sulfate in the cell. Rotaliid foraminifera are not only able to precipitate calcium carbonate but also to control its composition and mineralogy. Three non-mutually exclusive processes have been described for charged ion transport to the site of biomineralization: seawater leak, transmembrane transport and seawater vacuolization (e.g. Erez, 2003; Bentov et al., 2009; Nehrke et al., 2013).

The biomineralization site is isolated from seawater through an extension of the pseudopodial network, part of the cytoskeleton, that extends out of the test of the foraminifera (Erez, 2003). This site of calcification has been suggested to be possibly open to external seawater at times, generating direct leaks of seawater to the site of biomineralization (Nagai et al., 2018; Nehrke et al., 2013). As a result, seawater Ca, Mg and sulfate, but also inorganic phosphate and nitrate ions, would make it directly to the calcification site. Such a leak could also explain the rapid incorporation of ^{33}S-labeled sulfate in the test. If the leak evolves in time (Nagai et al., 2018), the highest level of incorporation of external seawater ions would occur during the formation of the POS and incipient calcite. In contrast, the transport of Ca through the cell membranes, the TMT (trans-membrane transport), would be very selective and only calcium would be expected to be delivered the site of biomineralization. Documented in coccolithophorids, TMT occurs in foraminifera as well (Gussone et al., 2006; Langer et al., 2006, 2009; Nehrke et al., 2013). Yet, foraminiferal calcite tends to be richer in trace elements, which would require a combination with direct incorporation of seawater (e.g. Nagai et al., 2018).

Another way to bring ions to the site of calcification is through the transport of seawater isolated in a portion of the membrane that detaches from the rest of the membrane and forms a vacuole full of seawater. The vacuole is transported all the way to the site of calcification as its pH and concentration in Ca, Dissolved Inorganic Carbon (DIC) and Mg are modified (Bentov et al., 2009; Bentov and Erez, 2006; Dellinger et al., 2018; Erez, 2003; Rollion-Bard and Erez, 2010; Weiner and Addadi, 2011). Vacuoles would also bring sulfate and magnesium, which would explain the rapid incorporation of ^{33}S into the test, and could carry nitrate and phosphate as well. In addition to transport as ions, Ca and DIC may be possibly transported as (high-Mg) amorphous calcium carbonate (Mg-ACC) granules (de Nooijer et al., 2009; Dubicka et al., 2023, 2025).

In any case, the active transport of sulfate across the cytoplasmic membrane is necessary to explain the moderate but significant incorporation of sulfate inside the cytoplasm. If vesicular transport is the main way ions are brought to the site of calcification, sulfate from seawater may enter the cell, from external or vacuolized seawater, via transmembrane proteins, possibly of the sulfate permease (SulP) group. Though to our knowledge these proteins have not yet been identified in foraminifera, they belong to a large, ubiquitous family of proteins found in all kingdoms of life (Piłsyk and Paszewski, 2009). Many of these proteins function by $SO_4^{2-} : H^+$ symport, but $SO_4^{2-} : HCO_3^-$, or more generally, anion:anion antiports have been reported for several homologues (Piłsyk and Paszewski, 2009). Such SulPs could enable the transport of sulfate across membranes, from the seawater to the cytosol, coherent with the global presence of ^{33}S in the cytoplasm and the organic matter (Figs. 7, 8, 10). If the presence of SulP antiport were to be confirmed, export of sulfate from the vacuoles could contribute to the increase of pH and DIC as the seawater evolves, suggesting that the sulfate remaining in the vacuole would be delivered to the test and that the removed sulfate would remain in the cytoplasm. However, we cannot access the occurrence of ^{33}S or the elemental composition of the vesicles that would have contained seawater or modified seawater. They now may be part of the vesicles that appear "empty", because the liquid inside them would have been lost during the chemical fixation. The process indeed removes all free ions and small molecules from the cytosol or from within the vacuoles and organelles. We are thus unable to identify possible seawater vacuoles and provide further information on the SWV model. Future work should employ cryo-fixation and cryo-NanoSIMS techniques to elucidate the function of vacuoles in the transport of seawater sulfate within the cytoplasm (via SulPs) and at the calcification site.

4.2 Sulfur and sulfate assimilation

Our protocol enables us the investigate the occurrence of labeled sulfur in the cell (Fig. 7). The cytoplasm visible in the chemically fixed specimens, or the cellular material that remained attached to the test, is systematically enriched in ^{33}S. The $\delta^{33}S$ values imply a mixing of $\sim 1/3$ labeled and $\sim 2/3$ non-labeled sulfur (Table 3, Fig. 7). Higher labeled sulfur concentration occurs when the chamber effectively grew in the labeled artificial seawater. Organic matter close to the test displays average $\delta^{33}S$ values between 1800 ‰ and 3000 ‰ (Table 3), which indicates that $\sim 1/4$ of the sulfur comes from labeled sulfate and was thus taken from seawater during the duration of the experiment. For specimens F5(2)B3 and F2A2 (Fig. 7), for which the cell has been preserved and analyzed, we found average $\delta^{33}S$ values of 1932 ± 36 (2σ) and 529 ± 6 (2σ). This would correspond to $\sim 1/4$ and ~ 7 % of sulfur that originates from sulfate taken from seawater during the experiment. The higher incorporation of seawater sulfate here might reflect the fact that F5(2)B3 was cultivated at twice the sulfate concentration of F2A2 (Thaler et al., 2023).

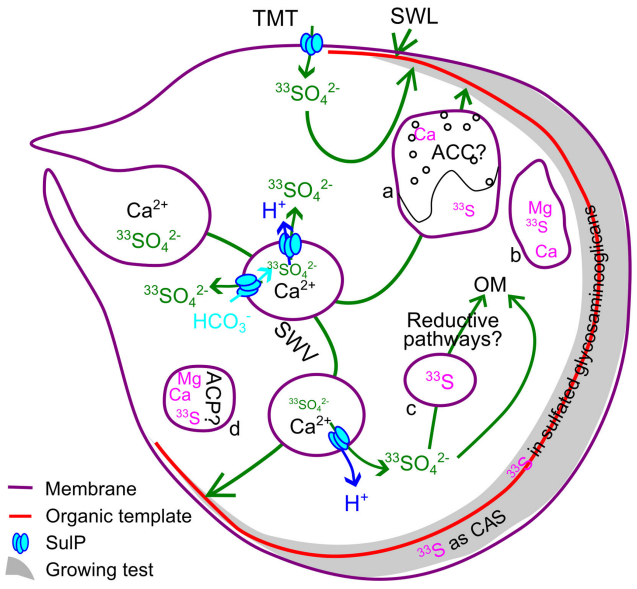


Figure 10. Schematic view of possible trajectories for labeled sulfur in the cell and co-occurrence with Mg, P and Ca. SulP = sulfate permease. SWL = seawater leak. TMT = trans-membrane transport. SWV = seawater vacuolization. ACC = Amorphous Calcium Carbonate. ACP = Amorphous Calcium Phosphate. a = vesicle containing Ca as ACC on one side and ^{33}S on the other. b = possible autophagosome. c = electron opaque body or fibrillar vesicle. d = possible acidocalcisome. In green, possible pathways for labeled sulfate. In pink, observed location of elements by NanoSIMS. In dark and light blue, possible SulP paths for protons and HCO_3^-. Sulfate crosses membranes through SulP channels together with protons, contributing to increase the Ca/Mg and the CO_3/SO_4 ratios of the vesicles as the composition of the fluid increases. Some of these vesicles might be associated to ACC formation. In the cytoplasm, labeled sulfur may be stored as sulfate in fibrillar vesicles or electron opaque bodies, and possibly reduced and/or incorporated as sulfate in organic molecules such as sulfated glycosaminoglycans. In the mineral part of the test, labeled sulfur delivered to the site of biomineralization is most likely included as Carbonate Associated Sulfate.

In those experiments, the labeled sulfur is necessarily initially introduced in the cell as a free sulfate ion, but the chemical fixation process applied to the cells removes small molecules and ions from the cell, such as ATP and free sulfate. Consequently, any remaining observable sulfur is thus either complexed or protein bound. In consequence, our estimates of the relative proportion of seawater sulfate-sulfur in the cell could be underestimated. Regardless of this partial loss of information, labeled sulfate is present in the cytoplasm, where it is transported and incorporated in less than two to five days (the duration of culture in the labeled medium), despite the provision of unlabeled food. Such an addition of seawater sulfate is coherent with its important physiological roles. Sulfate is one of the most important anions in cells and plays a key role in maintaining ionic homeostasis and other vital functions, and therefore is considered as an essential macronutrient (Piłsyk and Paszewski, 2009).

When labeled sulfur comes from food, we observe ^{33}S only in small grains within the cytoplasm. We also observe a lot of sulfur enrichment that is not labeled (Fig. 8). The labeled sulfur is found in grains that are always rich in phosphate and often in Mg, though most P-rich grains are independent from sulfur. An interpretation would be that sulfur from food travels through the cell in vacuoles that are not digested instantaneously, and that after 5 d, not all non-labeled food had been digested.

In our experiment, there are thus at least two sources of sulfur: sulfate pumped from seawater and dietary sulfur. The combination of ^{33}S and ^{34}S data suggests that a significant proportion of the sulfur in the cytoplasm originates from food or from seawater sulfate previously stored in internal pools similar to the ones suggested for inorganic carbon (ten Kuile and Erez, 1987, 1988). These account for at most 3/4 of the sulfur in the cytoplasm, even for foraminifera grown at higher sulfate concentrations (i.e., $[SO_4^{2-}] = 56.36$ mmol L^{-1} for F5(2)B). Our observation cannot confirm the occurrence of sulfate assimilatory reduction within the cell and because either seawater sulfate or food could have been ingested before the labeling experiments, some uncertainty remains in our interpretations.

Regardless, the presence of labeled sulfur in the cell is coherent with the fact that physiological activity of foraminifera, at least some benthic species, requires sulfate (Jauffrais et al., 2019; LeKieffre et al., 2022; Thaler et al., 2023) and within the cytoplasm of the cell, we observe ^{33}S-rich granular-like structures (white arrows Fig. 7). Sulfur enrichments in the kleptoplastic benthic foraminifera *Nonionellina labradorica*, as well as in *Bulimina marginata*, *Cassidulina laevigata*, *Haynesina germanica*, *Ammonia* sp. and *Elphidium williamsoni* have also been proposed to occur in fibrillar vesicles or electron-opaque bodies that also contain N (both smaller than 0.5 µm) or unidentified structures that are 2–5 µm big (LeKieffre et al., 2022). Here, the grains are smaller than 0.5 µm and could correspond to these fibrillar vesicles or electron opaque bodies previously described (Fig. 10). However, in addition to the inherent limitations of our fixation method, we cannot discriminate between reduced and oxidized sulfur and thus we cannot use our data to support the occurrence of sulfate assimilation observed in different species of foraminifera (Jauffrais et al., 2019; LeKieffre et al., 2022; Nomaki et al., 2016).

4.3 Ultrastructure of the test and element distribution: organic or inorganic banding?

In detail, two trends can be found in the correlations between those elements within the tests (Fig. 4) with S/Ca, P/Ca and Mg/Ca all varying simultaneously. Trend A is found across OCL_n and OCL_{n-1}, includes the presence of OOL_{n-1} (see Figs. 3 and 7) and most likely corresponds to the Mg-banding

that has been thoroughly investigated over the years (e.g., Eggins et al., 2004; Kunioka et al., 2006; Spero et al., 2015b; Fehrenbacher et al., 2017). Mg is inorganically present in foraminiferal calcite (Branson et al., 2013), which is expected due to its incorporation as an impurity in inorganic calcite, affecting calcite solubility and stability (Alkhatib et al., 2022; Mavromatis et al., 2013; Mucci, 1987; Saulnier et al., 2012). Occurrence of sulfate as an inorganic ion is expected as well, because sulfate is also incorporated in inorganically precipitated calcite (Barkan et al., 2020; Busenberg and Plummer, 1985; Fernández-Díaz et al., 2010; Goetschl et al., 2019; Kitano et al., 1975; Kontrec et al., 2004). The observed Mg-S covariation could be due to changes in precipitation rates, as higher rates translate into higher Mg- and SO_4-incorporation into the mineral lattice (Alkhatib et al., 2022; Barkan et al., 2020; Busenberg and Plummer, 1985; Mavromatis et al., 2013), though incorporation of sulfate reduces the possibility to incorporate magnesium (Goetschl et al., 2019). In this pattern, P variations could also be, at least partly, inorganically driven, as phosphate also is included in calcite as an impurity (House and Donaldson, 1986; Plant and House, 2002; Ren et al., 2021) and could track dissolved phosphate in seawater (Zhang et al., 2025). Though phosphorus is traditionally interpreted as reflecting the occurrence of organic matter, an unexpected observation remains that the OCL_n is overall more P-enriched than the OOL themselves. Indeed, the P, S and Mg enrichment is independent from the white lines observed in the TEM view.

Compared to trend A, trend B represents P, Mg and S enrichments across the POS and possibly extends into the OCL. It could be explained by the presence of organic matter that contains S, Mg and P. Sulfur is known to be present in sulfated glycosaminoglycans located in the POS (Angell, 1967; Bé et al., 1979; Dauphin et al., 2008; Hemleben et al., 1986; Spero, 1998; Weiner and Erez, 1984) and enrichment of Mg (and Na) in the POS of *O. universa* has been interpreted as a contribution of organically carried Mg (Branson et al., 2016), supporting earlier interpretation of an association of Mg to organic matter (Erez, 2003; Kunioka et al., 2006). In this case, trend B could be due to the co-occurrence of S, Mg and P in organic matter or the amorphous blobs observed in the POS This observation of a wide and irregular POS is consistent with previous investigations (e.g. Branson et al., 2016; Lemelle et al., 2020), though here we suggest that organic matter might not be the only common carrier. Indeed, the bright-field TEM views overall reveal amorphous/organic linings as thin white lines, the HAADF imaging reveals them as equally sharp less dense areas. Contrastingly, NanoSIMS maps follow a coherent but broader pattern that is not explainable by the difference of resolution between the methods (Fig. 6). Phosphorus, S and Mg define clearly areas broader than the white lines and the areas that are the most enriched in P, S and Mg appear centered on non-crystalline blobs within the POS (Figs. 2, 5, 6). The co-occurrence of P, S and Mg within and around the POS has already been demonstrated in foraminifera that have not undergone chemical fixation, including well preserved Quaternary fossils (Lemelle et al., 2020).

Within the outer calcitic layers (Figs. 5, 6), locally dark areas (less crystalline or with a different orientation) are associated with a transition from high to low P, Mg and S levels. In between those areas are P, Mg and S-rich zones associated with brighter zones, which seem to extend into the calcitic layer. However, HAADF-STEM observations reveal no detectable change in density, and thus probably not a change in OM content. Instead, they are more consistent with changes in crystallinity and/or crystal orientation and amount of impurity in calcite rather than a phase change. Altogether these observations support that S and Mg, and possibly P as well, reflect a combination of processes that include both inorganic incorporation in calcite and presence in organic matter as well as their contribution to amorphous biomineralization pathways. Furthermore, the use of composition maps without fine observations of test ultrastructure may lead to misinterpretation of S bandings as organic linings only. This conclusion however may not apply to the IOL that does appear to be the richest parts of the cell in both S and P (Fig. 8), though this is hard to properly constrain due to the obvious change in matrix from cytoplasm to test.

Overall, our observations could support that organic sulfur in the IOL, or the test is not sourced from food only. The lack of ^{33}S-poor banding in the test of chambers that grew in labeled seawater also supports that dietary sulfur does not play an important role in test building (Fig. 9). In Fig. 8, the chamber grew before foraminifer has been fed with labeled algae, which could explain the lack of labeled sulfur in the test. Contrastingly, the moderate, yet unambiguous presence of labeled sulfur in a test not grown in labeled seawater (Figs. 4, 5) suggests that some seawater-sulfur, unlike dietary sulfur, is incorporated in previously built chambers, which could suggest a renewing of the organic matter in older chambers and/or addition of new ions within the mineral lattice once the chamber is built.

4.4 Implication for biocalcification processes: Amorphous calcium carbonate pathway(s)?

Non-crystalline structures within the POS or the grains of the OCL could be grains of Amorphous Calcium Carbonate (ACC). ACC is a family of disordered phases more or less hydrated (Cartwright et al., 2012), likely to occur as a transitory precursor phase in many calcifying organisms, including foraminifera (Addadi et al., 2003; Arns et al., 2022; Bentov et al., 2010; De Yoreo et al., 2015; Dubicka et al., 2023; Gilbert et al., 2022; Jørgensen et al., 1985; Lemelle et al., 2020; de Nooijer et al., 2014; Weiner et al., 2003). Vaterite has also been suggested as a precursor to foraminiferal calcite (Jacob et al., 2017).

In addition to the presence of organic matter, the correlations between S/Ca, Mg/Ca and P/Ca in parts of the

test (profile 2 and 3, trend B) could reflect their combination in controlling ACC formation, stability and/or ACC-calcite transition. The co-occurrence of ACC and phosphorus could also be partly explained by the role of polyphosphate molecules, notably phospho-amino acids, that play a role in the induction of ACC formation in organisms such as crayfish (Bentov et al., 2010; Weiner et al., 2003). Phosphate could also occur as inorganic phosphate ions that can also promote the crystallization of calcite from ACC because they prevent vaterite formation (Zou et al., 2021). Calcium-phosphate grains could also be hypothesized to occur in the test, as a way to keep phosphate away from the growing calcite. Similarly, though Mg is likely to reduce the ability to form ACC at seawater Mg/Ca ratios (Evans et al., 2019), it increases the stability of ACC (Dubicka et al., 2023, 2025; Evans et al., 2020) and favors the formation of calcite over vaterite (Rodriguez-Blanco et al., 2012). Finally, sulfate as well plays many roles in controlling ACC or $CaCO_3$ minerals that precipitate, whether calcite or aragonite but also vaterite (Bots et al., 2012; Fernández-Díaz et al., 2010).

We thus hypothesize here that Mg and SO_4^{2-} all contribute to ACC formation, stabilization and/or evolution, possibly in association with phosphate as well, just like they do in calcite and aragonite precipitation. We also assume that they are all easily incorporated in ACC. For instance, Mg is incorporated in ACC twice as much as in calcite (Evans et al., 2020; Raz et al., 2000). The incorporation of sulfate in ACC formation is not documented yet, but the similarity of patterns with Mg and P could be due to the need to control them in the precipitation fluid and in the growing calcium carbonate. This could also explain why many elements, including S and Mg, are distributed more broadly than the POS, assuming that the stabilization of calcite implies progressive removal of the ionic impurities. Furthermore, the nanogranular structure we observe in the OCLs (Fig. 2), with a lower z (brighter STEM HAADF) and lower electron density (darker TEM) could possibly be interpreted as the occurrence of small ACC grains in the test, because such small grains can be observed within the OLs (Fig. 2e) and extend into the OCLs. Alternatively, they could be fluid inclusions within the test because the transition from ACC to calcite that will likely occur with a dehydration and decrease of volume (Bots et al., 2012; Cartwright et al., 2012). Other possible interpretations would be that they are Mg-rich nanodomains, similar to those observed in brittlestar Mg calcite, associated to the transition from ACC to calcite by spinodal decomposition (Polishchuk et al., 2017; Seknazi et al., 2019). In the lack of precise chemical compositions of those nanograins, much smaller than the resolution of the NanoSIMS, we cannot unambiguously conclude on the nature of those structures. Their occurrence is nonetheless highly consistent with non-classical biomineralization pathways in general, and with the presence of transitory ACC in particular.

In the cytoplasm, the presence of ACC could explain the Ca-rich vesicle observed in specimen F2A2 (Fig. 7i), as ACC is known to occur in 5 µm vesicles in *A. tepida* (de Nooijer et al., 2009) and *A. lessonii*, which have been suggested to be directly incorporated in the growing test Dubicka et al. (2023, 2025). We acknowledge that observation of ACC using our fixation protocol is unlikely because of the use of the Sörensen buffer solution. We have however no other interpretation to suggest for the concentration of calcium in this given vesicle. The putative grain of ACC (red arrow Figs. 7, 10), similar in size as observations from de Nooijer et al. (2009) or Dubicka et al. (2023, 2025), appears associated with S removal, as indicated by the separation between Ca and ^{33}S. In this scenario, the intervention of SulP proteins could remove sulfate and add carbonate or remove sulfate and protons. The vesicle below has a similar ^{33}S distribution and could also be interpreted as an ACC-containing vesicle, from which the ACC would have been removed during the fixation process. We also observe that Ca is often associated to P enrichment in the cytoplasm, but also with Mg (specimens F5(2)B and F2A2n Fig. 7 and individual Fa5B1 in Fig. 8). Such mutual Ca and P enrichments could be only analytical artifacts due to our protocol, which was not originally designed to observe the distribution of those elements within the cytoplasm. The use of the Sorensen -phosphate solution is likely to generate calcium phosphate precipitation, thus casting doubt on the meaning of Ca and P co-occurrence in our observations (Ayache et al., 2010; Docampo, 2023; Ingrid et al., 2025; Miranda et al., 2000). We also note occurrence of phosphate independent of calcium as well as the opposite, obscuring how much the distribution of these elements is due to our protocol. Instead, cryo-fixation would be more suited for the observation of small or soluble molecules (Ayache et al., 2010). This approach has enabled the observation of P-rich structures in *Ammonia veneta* and *Bolivina spissa* (Glock et al., 2025). In *B. spissa*, they were interpreted as granules of Ca polyphosphates. In *A. veneta*, P was found to accumulate in vesicles 0.5–2.0 µm in diameter, not unlike the size of what can be observed in the cell of F5(2)B3 (Fig. 7a–f) or F2A2 (Fig. 7g–l). Structures of similar size have been described as either acidocalcisomes or autophagosomes (Glock et al., 2025; Goodenough et al., 2019). The less regular structures observed in F5(2)B3 (green arrow) could correspond to autophagosomes, which are described as irregular in shape and accumulate Ca-polyphosphates (Docampo and Moreno, 2011; Glock et al., 2025). Smaller structures could correspond to acidocalcisomes that are close to 0.5 µm in size and accumulate granular phosphate and inorganic polyphosphate gels, as well as calcium as ACP (Amorphous Calcium Phosphate), magnesium and metals (Docampo et al., 2005). Unlike other soluble molecules, ACP could have been left intact by our protocol because it is less soluble at the conditions of the Sörensen-phosphate buffer solution ($[Ca] > 1\ mmol\ L^{-1}$; pH 7; Tung, 1998).

As a result, though our data on P distribution within the cytoplasm must be treated with caution, other published studies have demonstrated that foraminiferal cells contain or-

ganelles, such as acidocalcisome and autophagosome, which can store amorphous calcium phosphate and/or polyphosphate long chains in a gel or solid configuration (Glock et al., 2025; Goodenough et al., 2019). Thus, phosphate, often associated with calcium or magnesium, could be active in biomineralization processes of rotaliid foraminifera and play active roles as an inorganic ion, not only as a part of organic matter or ATP. This could include ACP, which has been demonstrated to play an important role in urchin spicule or coccolith calcite precipitation (Kahil et al., 2021). Taken together, our observations and previous studies could also suggest the occurrence of ACP in the test in combination to ACC, as another contributor to trend B and the P-enrichments observed in non-crystalline grains.

4.5 Implications for CAS as a proxy

Most (if not all) of the sulfate in the test comes ultimately from seawater, as supported by the ^{33}S labeling experience, whether through SWV, SWL or TMTs. Such a result, associated with small fractionation during carbonate precipitation (Barkan et al., 2020) contributes to explain why foraminifera appear as robust recorder of seawater $\delta^{34}S$ values (Burdett et al., 1989; Paris et al., 2014a; Rennie et al., 2018; Thaler et al., 2023). However, though the S/Ca ratio in foraminifera has been suggested to reflect seawater carbonate ion concentration (Boyle et al., 2002; van Dijk et al., 2017, 2019b), it is probably not linked to a direct precipitation from seawater itself, but instead might result from a complex mechanism, involving Ca-, Mg-, CO_3^{2-} and SO_4^{2-} control. In the absence of further constraints, and assuming that SulP are present in the cell, we could speculate that pH and DIC regulation necessary to calcite formation involves $SO_4^{2-} : H^+$ symport or $SO_4^{2-} : HCO_3^-$ antiport SulP proteins that could alter the SO_4/CO_3 content of the precipitating material to the initial seawater, as well as the Mg/Ca ratio, more or less depending on the initial seawater pH. Furthermore, the POS in tests that grew in labeled seawater does not appear to correspond to lower ^{33}S values, which suggests that the sulfate in the POS would also come from seawater, and not from the food. Thus, organically bound sulfate that occurs in the POS may also bear the $\delta^{34}S$ value of seawater, unless a fractionation is shown to occur as sulfate is incorporated into sulfated glycosaminoglycans. As a result, the sulfur isotope signature of CAS may be unaffected by the integration of the organic matter from the test itself. It could, however, be modified by the integration of OM from the cytoplasm, which contains reduced sulfur with a distinct isotopic signature (Thaler et al., 2023). Indeed, most (dissimilatory) sulfate reducing processes tend to generate lower isotopic $^{34}S/^{32}S$ ratios in the reduced product, which would imply that sulfur in organic matter has a lower $\delta^{34}S$ value than the initial sulfate available (e.g., Habicht et al., 2002; Farquhar et al., 2003; Crowe et al., 2014; Gomes and Hurtgen, 2015; Sim et al., 2023). As a result, removal of organic matter included within the test may be of lesser importance for the interpretation of $\delta^{34}S$ values than the removal of the cytoplasm.

5 Conclusion

Cells were cultured in ^{33}S-labeled seawater to document the origin of sulfur in the calcitic test and the cytoplasm of the rotaliid benthic foraminifera. Cells that lived in ^{33}S-labeled seawater revealed that at least 3/4 of the sulfur in the test comes from seawater sulfate. Thanks to a fixation process that gives access to both the test and the cytoplasm, we revealed that ^{33}S-labeled sulfur from seawater sulfate is found within the cytoplasm and the test. In addition, a combination of TEM bright-field, HAADF-STEM imaging and NanoSIMS analysis highlights the general co-occurrence of Mg, S and P according to the ultrastructure of the test chambers. These elements appear to be concentrated in two areas, primarily near the primary organic sheet (POS) and within the last-deposited outer calcitic layer. Non-crystalline grains can be found in the parts of the POS that are richest in P, Mg and S, and within the organic calcitic layers and could contain amorphous phases such as ACC. ^{33}S-labeled sulfur is present in a test that formed in seawater, indicating incorporation of seawater sulfate with calcium and carbonate ions, independently of the structure of the organic layers. This sulfur could be either inorganic or organic sulfate, or even possibly reduced sulfur in association with organic matter only. However, the absence of layering in the test suggests that this labeled sulfur is predominantly found within calcite itself, which is the most ubiquitous phase of the test. Finally, µm-scale grains can be found in the cytoplasm. A Ca-rich grain, approximately 3 µm large, can be interpreted as ACC-containing vesicle, while smaller grains (less than 1 µm) Ca, Mg and P rich and could be interpreted as structures that contain calcium in association with phosphate, possibly amorphous, such as acidocalcisomes or autophagosomes, though the method we used is not suited for their observation.

Sulfate incorporation and its occurrence at the sites of mineralization are thus most likely closely controlled by the cell. Such control might occur through Ca^{2+}or alkalinity pumps, that would decrease the relative abundance of sulfate compared to Ca^{2+} or CO_3^{2-} but could also involve active proteins, likely of the Sulfate permease family. Regulation of sulfate is necessary for foraminifera, possibly due to the assimilation of sulfate and to the control of the biomineral phase that precipitates. Indeed, sulfate also plays a role in precursor precipitation and stabilization. Together with magnesium and possibly phosphate, sulfate likely plays many roles in controlling ACC or the polymorphs of $CaCO_3$ that precipitate, whether calcite, and aragonite and even vaterite. SulP proteins could thus be involved in the evolution of seawater/biomineralizing fluid composition in vacuoles or at the sites of precipitation, to control the presence of sulfate in the POS, and the amount of sulfate in interaction with ACC or calcite. Though we can-

not confirm the occurrence of an assimilatory pathway for sulfur in foraminifera we investigated, the clear presence of sulfur from seawater in the cell demonstrates that sulfate is involved in many aspects of foraminifera biological activity, and likely with the formation and evolution of amorphous phases during biomineralization processes.

Data availability. All the original files of the TEM/STEM (https://doi.org/10.24396/ORDAR-230, Paris et al., 2026a) and NanoSIMS images and profiles (https://doi.org/10.24396/ORDAR-245, Paris et al., 2026b) used in this document are available online.

Supplement. The supplement related to this article is available online at https://doi.org/10.5194/bg-23-7911-2026-supplement.

Author contributions. AB, GP and CT designed the experiments and established the sequence of observations to perform. Growth experiments were led by CT and MD. NanoSIMS analyses and data processing were performed by CT, AB, JA, and SM. FIB sections were extracted by DT. TEM observations were performed by GYW, AB and CT. GP interpreted the data and wrote the paper with AB and with significant contributions from CT, MD, AAT, CRB and JA.

Competing interests. The contact author has declared that none of the authors has any competing interests.

Disclaimer. Publisher's note: Copernicus Publications remains neutral with regard to jurisdictional claims made in the text, published maps, institutional affiliations, or any other geographical representation in this paper. The authors bear the ultimate responsibility for providing appropriate place names. Views expressed in the text are those of the authors and do not necessarily reflect the views of the publisher.

Acknowledgements. We thank the editor as well as the two referees, referee 1 and Inge van Dijk, for their careful handling and useful reviews of this work. We thank Chakib Djediat and Géraldine Toutirais for their assistance with the chemical foraminiferal cell fixation and the acquisition of SEM images, respectively, at the Electron Microscopy Platform (PtME) of the Muséum national d'Histoire naturelle (MNHN), Paris, France. The National NanoSIMS facility is funded by CNRS, Région Île de France, Ministère délégué à l'Enseignement supérieur et à la Recherche, and the MNHN and is part of the RéGEF network. FIB experiments were supported by the French RENATECH network, the CPER Hauts de France project IMITECH and the Métropole Européenne de Lille.

Financial support. This research has been supported by the Centre National de la Recherche Scientifique, Institut national des sciences de l'Univers (grant no. Interrvie – Impact of sulfate variations on the biocalcification of foraminifera), by the LabEx BCDiv project (grant no. SULFOR, Impact of SO2on ocean acidification and foraminiferal biocalcification), by the Ile-de-France Région – DIM "Patrimoines matériels – innovation, expérimentation et resilience" (grant no. POLIMO – Projet d'Observation aux Limites des Interactions Minéral/Organique à l'échelle cellulaire).

Review statement. This paper was edited by Chiara Borrelli and reviewed by Inge van Dijk and one anonymous referee.

References

Addadi, L., Raz, S., and Weiner, S.: Taking Advantage of Disorder: Amorphous Calcium Carbonate and Its Roles in Biomineralization, Adv. Mater., 15, 959–970, https://doi.org/10.1002/adma.200300381, 2003.

Aléon-Toppani, A., Brunetto, R., Aléon, J., Dionnet, Z., Rubino, S., Levy, D., Troadec, D., Brisset, F., Borondics, F., and King, A.: A preparation sequence for multi-analysis of µm-sized extraterrestrial and geological samples, Meteorit. Planet. Sci., 56, 1151–1172, https://doi.org/10.1111/maps.13696, 2021.

Alkhatib, M., Qutob, M., Alkhatib, S., and Eisenhauer, A.: Influence of precipitation rate and temperature on the partitioning of magnesium and strontium in calcite overgrowths, Chem. Geol., 599, 120841, https://doi.org/10.1016/j.chemgeo.2022.120841, 2022.

Angell, R. W.: The Test Structure and Composition of the Foraminifer Rosalina floridana, J. Protozool., 14, 299–307, https://doi.org/10.1111/j.1550-7408.1967.tb02001.x, 1967.

Arns, A. I., Evans, D., Schiebel, R., Fink, L., Mezger, M., Alig, E., Linckens, J., Jochum, K. P., Schmidt, M. U., Jantschke, A., and Haug, G. H.: Mesocrystalline Architecture in Hyaline Foraminifer Shells Indicates a Non-Classical Crystallisation Pathway, Geochem. Geophy. Geosy., 23, e2022GC010445, https://doi.org/10.1029/2022GC010445, 2022.

Ayache, J., Beaunier, L., Boumendil, J., Ehret, G., and Laub, D.: Sample preparation handbook for transmission electron microscopy: methodology, Springer Science & Business Media, New York, ISBN 978-0-387-98181-9, https://doi.org/10.1007/978-0-387-98182-6, 2010.

Barkan, Y., Paris, G., Webb, S. M., Adkins, J. F., and Halevy, I.: Sulfur isotope fractionation between aqueous and carbonate-associated sulfate in abiotic calcite and aragonite, Geochim. Cosmochim. Ac., 280, 317–339, https://doi.org/10.1016/j.gca.2020.03.022, 2020.

Bé, A. W. H., Hemleben, C., Anderson, O. R., and Spindler, M.: Chamber Formation in Planktonic Foraminifera, Micropaleontology, 25, 294–307, https://doi.org/10.2307/1485304, 1979.

Bentov, S. and Erez, J.: Impact of biomineralization processes on the Mg content of foraminiferal shells: A biological perspective, Geochem. Geophy. Geosy., 7, Q01P08, https://doi.org/10.1029/2005gc001015, 2006.

Bentov, S., Brownlee, C., and Erez, J.: The role of seawater endocytosis in the biomineralization process in calcareous foraminifera, P. Natl. Acad. Sci. USA, 106, 21500–21504, https://doi.org/10.1073/pnas.0906636106, 2009.

Bentov, S., Weil, S., Glazer, L., Sagi, A., and Berman, A.: Stabilization of amorphous calcium carbonate by phosphate rich organic matrix proteins and by single phosphoamino acids, J. Struct.

Biol., 171, 207–215, https://doi.org/10.1016/j.jsb.2010.04.007, 2010.

Berner, R. A. and Canfield, D. E.: A new model for atmospheric oxygen over Phanerozoic time, Am. J. Sci., 289, 333, https://doi.org/10.2475/ajs.289.4.333, 1989.

Bots, P., Benning, L. G., Rickaby, R. E. M., and Shaw, S.: The role of SO_4 in the switch from calcite to aragonite seas, Geology, 39, 331–334, https://doi.org/10.1130/G31619.1, 2011.

Bots, P., Benning, L. G., Rodriguez-Blanco, J.-D., Roncal-Herrero, T., and Shaw, S.: Mechanistic Insights into the Crystallization of Amorphous Calcium Carbonate (ACC), Cryst. Growth Des., 12, 3806–3814, https://doi.org/10.1021/cg300676b, 2012.

Boyle, E., Berry, J., Erez, J., and Tishler, C.: Sulfur in foraminifera shells, a new paleoceanographic proxy for carbonate ion in seawater, AGU Fall Meeting Abstracts, PP52B-13, https://ui.adsabs.harvard.edu/abs/2002AGUFMPP52B..13B/abstract (last access: 23 October 2026), 2002.

Branson, O., Redfern, S. A. T., Tyliszczak, T., Sadekov, A., Langer, G., Kimoto, K., and Elderfield, H.: The coordination of Mg in foraminiferal calcite, Earth Planet. Sc. Let., 383, 134–141, https://doi.org/10.1016/j.epsl.2013.09.037, 2013.

Branson, O., Bonnin, E. A., Perea, D. E., Spero, H. J., Zhu, Z., Winters, M., Hönisch, B., Russell, A. D., Fehrenbacher, J. S., and Gagnon, A. C.: Nanometer-Scale Chemistry of a Calcite Biomineralization Template: Implications for Skeletal Composition and Nucleation, P. Natl. Acad. Sci. USA, 113, 12934–12939, https://doi.org/10.1073/pnas.1522864113, 2016.

Bryant, R. N., Richardson, J. A., Kalia, T. C., Gros, O., Lopez-Garriga, J., and Blättler, C. L.: Inorganic sulfate-based signatures of chemosymbiosis in modern infaunal lucinids, Geology, https://doi.org/10.1130/G51353.1, 2023.

Burdett, J. W., Arthur, M. A., and Richardson, M.: A Neogene seawater sulfur isotope age curve from calcareous pelagic microfossils, Earth Planet. Sc. Let., 94, 189–198, https://doi.org/10.1016/0012-821X(89)90138-6, 1989.

Burton, E. A. and Walter, L. M.: The role of pH in phosphate inhibition of calcite and aragonite precipitation rates in seawater, Geochim. Cosmochim. Ac., 54, 797–808, https://doi.org/10.1016/0016-7037(90)90374-T, 1990.

Busenberg, E. and Plummer, L. N.: Kinetic and thermodynamic factors controlling the distribution of SO_3^{2-} and Na^+ in calcites and selected aragonites, Geochim. Cosmochim. Ac., 49, 713–725, https://doi.org/10.1016/0016-7037(85)90166-8, 1985.

Canfield, D. E. and Raiswell, R.: The evolution of the sulfur cycle, Am. J. Sci., 299, 697–723, https://doi.org/10.2475/ajs.299.7-9.697, 1999.

Cartwright, J. H. E., Checa, A. G., Gale, J. D., Gebauer, D., and Sainz-Díaz, C. I.: Calcium Carbonate Polyamorphism and Its Role in Biomineralization: How Many Amorphous Calcium Carbonates Are There?, Angewandte Chemie International Edition, 51, 11960–11970, https://doi.org/10.1002/anie.201203125, 2012.

Claypool, G. E., Holser, W. T., Kaplan, I. R., Sakai, H., and Zak, I.: The age curves of sulfur and oxygen isotopes in marine sulfate and their mutual interpretation, Chem. Geol., 28, 199–260, https://doi.org/10.1016/0009-2541(80)90047-9, 1980.

Craddock, P. R., Rouxel, O. J., Ball, L. A., and Bach, W.: Sulfur isotope measurement of sulfate and sulfide by high-resolution MC-ICP-MS, Chem. Geol., 253, 102–113, https://doi.org/10.1016/j.chemgeo.2008.04.017, 2008.

Crowe, S. A., Paris, G., Katsev, S., Jones, C., Kim, S.-T., Zerkle, A. L., Nomosatryo, S., Fowle, D. A., Adkins, J. F., Sessions, A. L., Farquhar, J., and Canfield, D. E.: Sulfate was a trace constituent of Archean seawater, Science, 346, 735–739, https://doi.org/10.1126/science.1258966, 2014.

Cuif, J.-P., Dauphin, Y., Doucet, J., Salome, M., and Susini, J.: XANES mapping of organic sulfate in three scleractinian coral skeletons, Geochim. Cosmochim. Ac., 67, 75–83, https://doi.org/10.1016/S0016-7037(02)01041-4, 2003.

Cusack, M., Dauphin, Y., Cuif, J.-P., Salomé, M., Freer, A., and Yin, H.: Micro-XANES mapping of sulphur and its association with magnesium and phosphorus in the shell of the brachiopod, Terebratulina retusa, Chem. Geol., 253, 172–179, https://doi.org/10.1016/j.chemgeo.2008.05.007, 2008.

Dauphin, Y., Cuif, J.-P., Doucet, J., Salomé, M., Susini, J., and Terry Willams, C.: In situ chemical speciation of sulfur in calcitic biominerals and the simple prism concept, J. Struct. Biol., 142, 272–280, https://doi.org/10.1016/S1047-8477(03)00054-6, 2003.

Dauphin, Y., Cuif, J.-P., Salomé, M., and Susini, J.: Speciation and distribution of sulfur in a mollusk shell as revealed by in situ maps using X-ray absorption near-edge structure (XANES) spectroscopy at the S K-edge, Am. Mineral., 90, 1748–1758, https://doi.org/10.2138/am.2005.1640, 2005.

Dauphin, Y., Cuif, J.-P., and Williams, C. T.: Soluble organic matrices of aragonitic skeletons of Merulinidae (Cnidaria, Anthozoa), Comp. Biochem. Phys. B, 150, 10–22, https://doi.org/10.1016/j.cbpb.2008.01.002, 2008.

Dauphin, Y., Ball, A. D., Castillo-Michel, H., Chevallard, C., Cuif, J.-P., Farre, B., Pouvreau, S., and Salomé, M.: In situ distribution and characterization of the organic content of the oyster shell Crassostrea gigas (Mollusca, Bivalvia), Micron, 44, 373–383, https://doi.org/10.1016/j.micron.2012.09.002, 2013.

Dellinger, M., West, A. J., Paris, G., Adkins, J. F., Pogge von Strandmann, P. A. E., Ullmann, C. V., Eagle, R. A., Freitas, P., Bagard, M.-L., Ries, J. B., Corsetti, F. A., Perez-Huerta, A., and Kampf, A. R.: The Li isotope composition of marine biogenic carbonates: Patterns and mechanisms, Geochim. Cosmochim. Ac., 236, 315–335, https://doi.org/10.1016/j.gca.2018.03.014, 2018.

de Nooijer, L. J., Langer, G., Nehrke, G., and Bijma, J.: Physiological controls on seawater uptake and calcification in the benthic foraminifer *Ammonia tepida*, Biogeosciences, 6, 2669–2675, https://doi.org/10.5194/bg-6-2669-2009, 2009.

de Nooijer, L. J., Spero, H. J., Erez, J., Bijma, J., and Reichart, G. J.: Biomineralization in perforate foraminifera, Earth-Sci. Rev., 135, 48–58, https://doi.org/10.1016/j.earscirev.2014.03.013, 2014.

De Yoreo, J. J., Gilbert, P. U. P. A., Sommerdijk, N. A. J. M., Penn, R. L., Whitelam, S., Joester, D., Zhang, H., Rimer, J. D., Navrotsky, A., Banfield, J. F., Wallace, A. F., Michel, F. M., Meldrum, F. C., Cölfen, H., and Dove, P. M.: Crystallization by particle attachment in synthetic, biogenic, and geologic environments, Science, 349, aaa6760, https://doi.org/10.1126/science.aaa6760, 2015.

Docampo, R.: Advances in the cellular biology, biochemistry, and molecular biology of acidocalcisomes, Microbiol. Mol. Biol. R., 88, e00042-23, https://doi.org/10.1128/mmbr.00042-23, 2023.

Docampo, R. and Moreno, S. N. J.: Acidocalcisomes, Cell Calcium, 50, 113–119, https://doi.org/10.1016/j.ceca.2011.05.012, 2011.

Docampo, R., de Souza, W., Miranda, K., Rohloff, P., and Moreno, S. N. J.: Acidocalcisomes? conserved from bacteria to man, Nat. Rev. Microbiol., 3, 251–261, https://doi.org/10.1038/nrmicro1097, 2005.

Dubicka, Z., Bojanowski, M. J., Bijma, J., and Bickmeyer, U.: Mg-rich amorphous to Mg-low crystalline $CaCO_3$ pathway in foraminifera, Heliyon, 9, https://doi.org/10.1016/j.heliyon.2023.e18331, 2023.

Dubicka, Z., Syczewski, M. D., Benning, L. G., Schreiber, A., Wirth, R., Witkowski, M., Bojanowski, M. J., Pałczyńska, A., Janse, M., and Bickmeyer, U.: Amorphous calcium carbonate loaded multilamellar vesicles within Amphistegina (Rotaliida) foraminifera, Acta Biomater., 208, 525–537, https://doi.org/10.1016/j.actbio.2025.10.060, 2025.

Eggins, S. M., Sadekov, A., and De Deckker, P.: Modulation and daily banding of Mg/Ca in Orbulina universa tests by symbiont photosynthesis and respiration: a complication for seawater thermometry?, Earth Planet. Sc. Let., 225, 411–419, https://doi.org/10.1016/j.epsl.2004.06.019, 2004.

Erez, J.: The Source of Ions for Biomineralization in Foraminifera and Their Implications for Paleoceanographic Proxies, Rev. Mineral. Geochem., 54, 115–149, https://doi.org/10.2113/0540115, 2003.

Evans, D., Webb, P. B., Penkman, K., Kröger, R., and Allison, N.: The Characteristics and Biological Relevance of Inorganic Amorphous Calcium Carbonate (ACC) Precipitated from Seawater, Cryst. Growth Des., 19, 4300–4313, https://doi.org/10.1021/acs.cgd.9b00003, 2019.

Evans, D., Gray, W. R., Rae, J. W. B., Greenop, R., Webb, P. B., Penkman, K., Kröger, R., and Allison, N.: Trace and major element incorporation into amorphous calcium carbonate (ACC) precipitated from seawater, Geochim. Cosmochim. Ac., 290, 293–311, https://doi.org/10.1016/j.gca.2020.08.034, 2020.

Fakhraee, M., Crowe, S. A., and Katsev, S.: Sedimentary sulfur isotopes and Neoarchean ocean oxygenation, Sci. Adv., 4, e1701835, https://doi.org/10.1126/sciadv.1701835, 2018.

Falini, G., Albeck, S., Weiner, S., and Addadi, L.: Control of Aragonite or Calcite Polymorphism by Mollusk Shell Macromolecules, Science, 271, 67–69, https://doi.org/10.1126/science.271.5245.67, 1996.

Farquhar, J., Johnston, D. T., Wing, B. A., Habicht, K. S., Canfield, D. E., Airieau, S., and Thiemens, M. H.: Multiple sulphur isotopic interpretations of biosynthetic pathways: implications for biological signatures in the sulphur isotope record, Geobiology, 1, 27–36, https://doi.org/10.1046/j.1472-4669.2003.00007.x, 2003.

Fehrenbacher, J. S., Russell, A. D., Davis, C. V., Gagnon, A. C., Spero, H. J., Cliff, J. B., Zhu, Z., and Martin, P.: Link between light-triggered Mg-banding and chamber formation in the planktic foraminifera Neogloboquadrina dutertrei, Nat. Commun., 8, 15441, https://doi.org/10.1038/ncomms15441, 2017.

Fernández-Díaz, L., Fernández-González, Á., and Prieto, M.: The role of sulfate groups in controlling $CaCO_3$ polymorphism, Geochim. Cosmochim. Ac., 74, 6064–6076, https://doi.org/10.1016/j.gca.2010.08.010, 2010.

Gabitov, R. I., Wynn, P. M., Wearing, C., Carlson, L., Ariunbold, G., Jimenez-Arroyo, A. L., Bell, E., Halcovitch, N., and Thirumalai, R. V. K. G.: Uptake of ammonium and nitrate by calcium carbonate polymorphs, Geochim. Cosmochim. Ac., 421, 391–402, https://doi.org/10.1016/j.gca.2026.03.032, 2026.

Geerken, E., de Nooijer, L. J., Roepert, A., Polerecky, L., King, H. E., and Reichart, G. J.: Element banding and organic linings within chamber walls of two benthic foraminifera, Scientific Reports, 9, 3598, https://doi.org/10.1038/s41598-019-40298-y, 2019.

Gilbert, P. U. P. A., Bergmann, K. D., Boekelheide, N., Tambutté, S., Mass, T., Marin, F., Adkins, J. F., Erez, J., Gilbert, B., Knutson, V., Cantine, M., Hernández, J. O., and Knoll, A. H.: Biomineralization: Integrating mechanism and evolutionary history, Science Advances, 8, eabl9653, https://doi.org/10.1126/sciadv.abl9653, 2022.

Glock, N., Liebetrau, V., Vogts, A., and Eisenhauer, A.: Organic Heterogeneities in Foraminiferal Calcite Traced Through the Distribution of N, S, and I Measured With NanoSIMS: A New Challenge for Element-Ratio-Based Paleoproxies?, Front. Earth Sci., 7, https://doi.org/10.3389/feart.2019.00175, 2019.

Glock, N., Richirt, J., Woehle, C., Algar, C., Armstrong, M., Eichner, D., Firrincieli, H., Makabe, A., Govindankutty Menon, A., Ishitani, Y., Hackl, T., Hubert-Huard, R., Kienast, M., Milker, Y., Mutzberg, A., Ni, S., Okada, S., Rakshit, S., Schmiedl, G., Steiner, Z., Tame, A., Zhang, Z., and Nomaki, H.: Widespread occurrence and relevance of phosphate storage in foraminifera, Nature, 638, 1000–1006, https://doi.org/10.1038/s41586-024-08431-8, 2025.

Goetschl, K. E., Purgstaller, B., Dietzel, M., and Mavromatis, V.: Effect of sulfate on magnesium incorporation in low-magnesium calcite, Geochim. Cosmochim. Ac., 265, 505–519, https://doi.org/10.1016/j.gca.2019.07.024, 2019.

Gomes, M. L. and Hurtgen, M. T.: Sulfur isotope fractionation in modern euxinic systems: Implications for paleoenvironmental reconstructions of paired sulfate–sulfide isotope records, Geochim. Cosmochim. Ac., 157, 39–55, https://doi.org/10.1016/j.gca.2015.02.031, 2015.

Gomes, M. L., Hurtgen, M. T., and Sageman, B. B.: Biogeochemical sulfur cycling during Cretaceous oceanic anoxic events: A comparison of OAE1a and OAE2, Paleoceanography, 31, 233–251, https://doi.org/10.1002/2015PA002869, 2016.

Goodenough, U., Heiss, A. A., Roth, R., Rusch, J., and Lee, J.-H.: Acidocalcisomes: Ultrastructure, Biogenesis, and Distribution in Microbial Eukaryotes, Protist, 170, 287–313, https://doi.org/10.1016/j.protis.2019.05.001, 2019.

Gussone, N., Langer, G., Thoms, S., Nehrke, G., Eisenhauer, A., Riebesell, U., and Wefer, G.: Cellular calcium pathways and isotope fractionation in Emiliania huxleyi, Geology, 34, 625–628, https://doi.org/10.1130/G22733.1, 2006.

Habicht, K. S., Gade, M., Thamdrup, B., Berg, P., and Canfield, D. E.: Calibration of Sulfate Levels in the Archean Ocean, Science, 298, 2372–2374, https://doi.org/10.1126/science.1078265, 2002.

He, M., Yu, X., Deng, W., Chen, X., Peng, X., Ta, K., Xu, H., Cui, Z., Yang, Q., Yang, Y., Zhang, Y., and Wei, G.: In Situ Analysis of Sulfur Isotopic Fractionation in Deep-Sea Corals Using Secondary-Ion Mass Spectrometry: Insights Into

Vital Effects, J. Geophys. Res.-Biogeo., 129, e2024JG008032, https://doi.org/10.1029/2024JG008032, 2024.

Hemleben, C., Be, A. W. H., Anderson, O. R., and Tuntivate, S.: Test morphology, organic layers and chamber formation of the planktonic foraminifer Globorotalia menardii (d'Orbigny), J. Foramin. Res., 7, 1–25, https://doi.org/10.2113/gsjfr.7.1.1, 1977.

Hemleben, C., Erson, O., Berthold, W., and Spindler, M.: Calcification and chamber formation in Foraminifera-a brief overview, Biomineralization in lower plants and animals (BSC Leadbeater, R Riding, eds) Clarendon Press, Oxford, 237–249, https://www.researchgate.net/publication/230889924_Calcification_and_chamber_formation_in_Foraminifera_-_a_brief_overview (last access: 23 October 2026), 1986.

Hofmann, S., Voïtchovsky, K., Spijker, P., Schmidt, M., and Stumpf, T.: Visualising the molecular alteration of the calcite (104) – water interface by sodium nitrate, Scientific Reports, 6, 21576, https://doi.org/10.1038/srep21576, 2016.

Horita, J., Zimmermann, H., and Holland, H. D.: Chemical evolution of seawater during the Phanerozoic: Implications from the record of marine evaporites, Geochim. Cosmochim. Ac., 66, 3733–3756, 2002.

House, W. A.: Inhibition of calcite crystal growth by inorganic phosphate, J. Colloid Interf. Sci., 119, 505–511, https://doi.org/10.1016/0021-9797(87)90296-7, 1987.

House, W. A. and Donaldson, L.: Adsorption and coprecipitation of phosphate on calcite, J. Colloid Interf. Sci., 112, 309–324, https://doi.org/10.1016/0021-9797(86)90101-3, 1986.

Ingrid, A., Moara, L., Wendell, G.-D., Anchieta, O. F. J. de, G., P. P., Wanderley, de S., and Kildare, M.: New dimensions in acidocalcisome research: the potential of cryo-EM to uncover novel aspects of protozoan parasite physiology, mBio, 16, e01662-24, https://doi.org/10.1128/mbio.01662-24, 2025.

Jacob, D. E., Wirth, R., Agbaje, O. B. A., Branson, O., and Eggins, S. M.: Planktic foraminifera form their shells via metastable carbonate phases, Nat. Commun., 8, 1265, https://doi.org/10.1038/s41467-017-00955-0, 2017.

Jauffrais, T., LeKieffre, C., Schweizer, M., Geslin, E., Metzger, E., Bernhard, J. M., Jesus, B., Filipsson, H. L., Maire, O., and Meibom, A.: Kleptoplastidic benthic foraminifera from aphotic habitats: insights into assimilation of inorganic C, N and S studied with sub-cellular resolution, Environ. Microbiol., 21, 125–141, https://doi.org/10.1111/1462-2920.14433, 2019.

Jørgensen, B. B., Erez, J., Revsbech, P., and Cohen, Y.: Symbiotic photosynthesis in a planktonic foraminiferan, Globigerinoides sacculifer (Brady), studied with microelectrodes, Limnol. Oceanogr., 30, 1253–1267, https://doi.org/10.4319/lo.1985.30.6.1253, 1985.

Kah, L. C., Lyons, T. W., and Frank, T. D.: Low marine sulphate and protracted oxygenation of the Proterozoic biosphere, Nature, 431, 834–838, https://doi.org/10.1038/nature02974, 2004.

Kahil, K., Weiner, S., Addadi, L., and Gal, A.: Ion Pathways in Biomineralization: Perspectives on Uptake, Transport, and Deposition of Calcium, Carbonate, and Phosphate, J. Am. Chem. Soc., 143, 21100–21112, https://doi.org/10.1021/jacs.1c09174, 2021.

Kampschulte, A., Bruckschen, P., and Strauss, H.: The sulphur isotopic composition of trace sulphates in Carboniferous brachiopods: implications for coeval seawater, correlation with other geochemical cycles and isotope stratigraphy, Chem. Geol., 175, 149–173, https://doi.org/10.1016/S0009-2541(00)00367-3, 2001.

Kester, D. R., Duedall, I. W., Connors, D. N., and Pytkowicz, R. M.: Preparation of artificial seawater, Limnol. Oceanogr., 12, 176–179, https://doi.org/10.4319/lo.1967.12.1.0176, 1967.

Kitano, Y., Okumura, M., and Idogaki, M.: Incorporation of sodium, chloride and sulfate with calcium carbonate, Geochem. J, 9, 75–84, 1975.

Kontrec, J., Kralj, D., Brečević, L., Falini, G., Fermani, S., Noethig-Laslo, V., and Mirosavljević, K.: Incorporation of Inorganic Anions in Calcite, Eur. J. Inorg. Chem., 2004, 4579–4585, https://doi.org/10.1002/ejic.200400268, 2004.

Kopp, C., Domart-Coulon, I., Escrig, S., Humbel, B. M., Hignette, M., and Meibom, A.: Subcellular Investigation of Photosynthesis-Driven Carbon Assimilation in the Symbiotic Reef Coral Pocillopora damicornis, mBio, 6, 10.1128/mbio.02299-14, https://doi.org/10.1128/mbio.02299-14, 2015.

Kunioka, D., Shirai, K., Takahata, N., Sano, Y., Toyofuku, T., and Ujiie, Y.: Microdistribution of Mg/Ca, Sr/Ca, and Ba/Ca ratios in Pulleniatina obliquiloculata test by using a NanoSIMS: Implication for the vital effect mechanism, Geochem. Geophy. Geosy., 7, https://doi.org/10.1029/2006GC001280, 2006.

LaFlamme, C., Barré, G., Fiorentini, M. L., Beaudoin, G., Occhipinti, S., and Bell, J.: A significant seawater sulfate reservoir at 2.0 Ga determined from multiple sulfur isotope analyses of the Paleoproterozoic Degrussa Cu-Au volcanogenic massive sulfide deposit, Western Australia, Geochim. Cosmochim. Ac., 295, 178–193, https://doi.org/10.1016/j.gca.2020.12.018, 2021.

Langer, G., Gussone, N., Nehrke, G., Riebesell, U., Eisenhauer, A., Kuhnert, H., Rost, B., Trimborn, S., and Thoms, S.: Coccolith strontium to calcium ratios in Emiliania huxleyi: The dependence on seawater strontium and calcium concentrations, Limnol. Oceanogr., 51, 310–320, https://doi.org/10.4319/lo.2006.51.1.0310, 2006.

Langer, G., Nehrke, G., Thoms, S., and Stoll, H.: Barium partitioning in coccoliths of Emiliania huxleyi, Geochim. Cosmochim. Ac., 73, 2899–2906, https://doi.org/10.1016/j.gca.2009.02.025, 2009.

Langer, M. R.: Biosynthesis of glycosaminoglycans in foraminifera: A review, Mar. Micropaleontol., 19, 245–255, https://doi.org/10.1016/0377-8398(92)90031-E, 1992.

LeKieffre, C., Bernhard, J. M., Mabilleau, G., Filipsson, H. L., Meibom, A., and Geslin, E.: An overview of cellular ultrastructure in benthic foraminifera: New observations of rotalid species in the context of existing literature, Mar. Micropaleontol., 138, 12–32, https://doi.org/10.1016/j.marmicro.2017.10.005, 2018.

LeKieffre, C., Jauffrais, T., Bernhard, J. M., Filipsson, H. L., Schmidt, C., Roberge, H., Maire, O., Panieri, G., Geslin, E., and Meibom, A.: Ammonium and Sulfate Assimilation Is Widespread in Benthic Foraminifera, Frontiers in Marine Science, 9, https://doi.org/10.3389/fmars.2022.861945, 2022.

Lemelle, L., Bartolini, A., Simionovici, A., Tucoulou, R., De Nolf, W., Bassinot, F., and de Garidel-Thoron, T.: Nanoscale trace metal imprinting of biocalcification of planktic foraminifers by Toba's super-eruption, Scientific Reports, 10, 10974, https://doi.org/10.1038/s41598-020-67481-w, 2020.

Lin, Y.-P. and Singer, P. C.: Inhibition of calcite precipitation by orthophosphate: Speciation and thermodynamic

considerations, Geochim. Cosmochim. Ac., 70, 2530–2539, https://doi.org/10.1016/j.gca.2006.03.002, 2006.

Loeblich, A. R. and Tappan, H.: Foraminiferal genera and their classification, Van Nostrand Reinhold Co., New York, 970 pp., https://doi.org/10.1007/978-1-4899-5760-3, 1987.

Lorens, R. B. and Bender, M. L.: The impact of solution chemistry on Mytilus edulis calcite and aragonite, Geochim. Cosmochim. Ac., 44, 1265–1278, https://doi.org/10.1016/0016-7037(80)90087-3, 1980.

Mavromatis, V., Gautier, Q., Bosc, O., and Schott, J.: Kinetics of Mg partition and Mg stable isotope fractionation during its incorporation in calcite, Geochim. Cosmochim. Ac., 114, 188–203, https://doi.org/10.1016/j.gca.2013.03.024, 2013.

Miranda, K., Benchimol, M., Docampo, R., and de Souza, W.: The fine structure of acidocalcisomes in Trypanosoma cruzi, Parasitol. Res., 86, 373–384, https://doi.org/10.1007/s004360050682, 2000.

Mucci, A.: Influence of temperature on the composition of magnesian calcite overgrowths precipitated from seawater, Geochim. Cosmochim. Ac., 51, 1977–1984, https://doi.org/10.1016/0016-7037(87)90186-4, 1987.

Nagai, Y., Uematsu, K., Chen, C., Wani, R., Tyszka, J., and Toyofuku, T.: Weaving of biomineralization framework in rotaliid foraminifera: implications for paleoceanographic proxies, Biogeosciences, 15, 6773–6789, https://doi.org/10.5194/bg-15-6773-2018, 2018.

Nehrke, G., Keul, N., Langer, G., de Nooijer, L. J., Bijma, J., and Meibom, A.: A new model for biomineralization and trace-element signatures of Foraminifera tests, Biogeosciences, 10, 6759–6767, https://doi.org/10.5194/bg-10-6759-2013, 2013.

Nomaki, H., Bernhard, J. M., Ishida, A., Tsuchiya, M., Uematsu, K., Tame, A., Kitahashi, T., Takahata, N., Sano, Y., and Toyofuku, T.: Intracellular Isotope Localization in Ammonia sp. (Foraminifera) of Oxygen-Depleted Environments: Results of Nitrate and Sulfate Labeling Experiments, Front. Microbiol., Volume 7, https://doi.org/10.3389/fmicb.2016.00163, 2016.

Oae, S.: Organic chemistry of sulfur, Springer Science & Business Media, https://doi.org/10.1007/978-1-4684-2049-4, 2012.

Ohkouchi, N., Kawamura, K., Kajiwara, Y., Wada, E., Okada, M., Kanamatsu, T., and Taira, A.: Sulfur isotope records around Livello Bonarelli (northern Apennines, Italy) black shale at the Cenomanian-Turonian boundary, Geology, 27, 535, https://doi.org/10.1130/0091-7613(1999)027<0535:SIRALB>2.3.CO;2, 1999.

Osburn, M. R., Owens, J., Bergmann, K. D., Lyons, T. W., and Grotzinger, J. P.: Dynamic changes in sulfate sulfur isotopes preceding the Ediacaran Shuram Excursion, Geochim. Cosmochim. Ac., 170, 204–224, https://doi.org/10.1016/j.gca.2015.07.039, 2015.

Paris, G., Sessions, A. L., Subhas, A. V., and Adkins, J. F.: MC-ICP-MS measurement of δ^{34}S and Δ^{33}S in small amounts of dissolved sulfate, Chem. Geol., 345, 50–61, https://doi.org/10.1016/j.chemgeo.2013.02.022, 2013.

Paris, G., Fehrenbacher, J. S., Sessions, A. L., Spero, H. J., and Adkins, J. F.: Experimental determination of carbonate-associated sulfate δ^{34}S in planktonic foraminifera shells, Geochem. Geophy. Geosy., 15, 1452–1461, https://doi.org/10.1002/2014gc005295, 2014a.

Paris, G., Adkins, J. F., Sessions, A. L., Webb, S. M., and Fischer, W. W.: Neoarchean carbonate–associated sulfate records positive Δ^{33}S anomalies, Science, 346, 739–741, https://doi.org/10.1126/science.1258211, 2014b.

Paris, G., Fischer, W. W., Johnson, J. E., Webb, S. M., Present, T. M., Sessions, A. L., and Adkins, J. F.: Deposition of sulfate aerosols with positive Δ^{33}S in the Neoarchean, Geochim. Cosmochim. Ac., 285, 1–20, https://doi.org/10.1016/j.gca.2020.06.028, 2020.

Paris, G., Thaler, C., Dellinger, M., Aléon, J., Mostefaoui, S., Aléon-Toppani, A., Rollion-Bard, C., Troadec, D., Wang, G. Y., and Bartolini, A.: Tracking sulfate, magnesium, phosphorus and amorphous phases in Rosalina-like benthic foraminifera – TEM data, OTELO [data set], https://doi.org/10.24396/ORDAR-230, 2026a.

Paris, G., Thaler, C., Dellinger, M., Aléon, J., Mostefaoui, S., Aléon-Toppani, A., Rollion-Bard, C., Troadec, D., Wang, G. Y., and Bartolini, A.: Tracking sulfate, magnesium, phosphorus and amorphous phases in Rosalina-like benthic foraminifera – NanoSIMS data, OTELO [data set], https://doi.org/10.24396/ORDAR-245, 2026b.

Patron, N. J., Durnford, D. G., and Kopriva, S.: Sulfate assimilation in eukaryotes: fusions, relocations and lateral transfers, BMC Evolutionary Biology, 8, 39, https://doi.org/10.1186/1471-2148-8-39, 2008.

Paytan, A., Kastner, M., Campbell, D., and Thiemens, M. H.: Sulfur Isotopic Composition of Cenozoic Seawater Sulfate, Science, 282, 1459–1462, https://doi.org/10.1126/science.282.5393.1459, 1998.

Piłsyk, S. and Paszewski, A.: Sulfate permeases – phylogenetic diversity of sulfate transport, Acta Biochim. Pol., 56, https://doi.org/10.18388/abp.2009_2470, 2009.

Plant, L. J. and House, W. A.: Precipitation of calcite in the presence of inorganic phosphate, Colloid. Surface. A, 203, 143–153, https://doi.org/10.1016/S0927-7757(01)01089-5, 2002.

Polishchuk, I., Bracha, A. A., Bloch, L., Levy, D., Kozachkevich, S., Etinger-Geller, Y., Kauffmann, Y., Burghammer, M., Giacobbe, C., Villanova, J., Hendler, G., Sun, C.-Y., Giuffre, A. J., Marcus, M. A., Kundanati, L., Zaslansky, P., Pugno, N. M., Gilbert, P. U. P. A., Katsman, A., and Pokroy, B.: Coherently aligned nanoparticles within a biogenic single crystal: A biological prestressing strategy, Science, 358, 1294–1298, https://doi.org/10.1126/science.aaj2156, 2017.

Present, T. M., Paris, G., Burke, A., Fischer, W. W., and Adkins, J. F.: Large Carbonate Associated Sulfate isotopic variability between brachiopods, micrite, and other sedimentary components in Late Ordovician strata, Earth Planet. Sc. Let., 432, 187–198, https://doi.org/10.1016/j.epsl.2015.10.005, 2015.

Present, T. M., Adkins, J. F., and Fischer, W. W.: Variability in Sulfur Isotope Records of Phanerozoic Seawater Sulfate, Geophys. Res. Lett., 47, e2020GL088766, https://doi.org/10.1029/2020GL088766, 2020.

Raz, S., Weiner, S., and Addadi, L.: Formation of High-Magnesian Calcites via an Amorphous Precursor Phase: Possible Biological Implications, Adv. Mater., 12, 38–42, https://doi.org/10.1002/(SICI)1521-4095(200001)12:1<38::AID-ADMA38>3.0.CO;2-I, 2000.

Rees, C. E., Jenkins, W. J., and Monster, J.: The sulphur isotopic composition of ocean water sulphate, Geochim. Cosmochim.

Ac., 42, 377–381, https://doi.org/10.1016/0016-7037(78)90268-5, 1978.

Ren, C., Li, Y., Zhou, Q., and Li, W.: Phosphate uptake by calcite: Constraints of concentration and pH on the formation of calcium phosphate precipitates, Chem. Geol., 579, 120365, https://doi.org/10.1016/j.chemgeo.2021.120365, 2021.

Rennie, V. C. F., Paris, G., Sessions, A. L., Abramovich, S., Turchyn, A. V., and Adkins, J. F.: Cenozoic record of δ^{34}S in foraminiferal calcite implies an early Eocene shift to deep-ocean sulfide burial, Nat. Geosci., https://doi.org/10.1038/s41561-018-0200-y, 2018.

Richardson, J. A., Newville, M., Lanzirotti, A., Webb, S. M., Rose, C. V., Catalano, J. G., and Fike, D. A.: Depositional and diagenetic constraints on the abundance and spatial variability of carbonate-associated sulfate, Chem. Geol., 523, 59–72, https://doi.org/10.1016/j.chemgeo.2019.05.036, 2019a.

Richardson, J. A., Newville, M., Lanzirotti, A., Webb, S. M., Rose, C. V., Catalano, J. G., and Fike, D. A.: The source of sulfate in brachiopod calcite: Insights from μ-XRF imaging and XANES spectroscopy, Chem. Geol., 529, 119328, https://doi.org/10.1016/j.chemgeo.2019.119328, 2019b.

Richardson, J. A., Lepland, A., Hints, O., Prave, A. R., Gilhooly, W. P., Bradley, A. S., and Fike, D. A.: Effects of early marine diagenesis and site-specific depositional controls on carbonate-associated sulfate: Insights from paired S and O isotopic analyses, Chem. Geol., 584, 120525, https://doi.org/10.1016/j.chemgeo.2021.120525, 2021.

Rodriguez-Blanco, J. D., Shaw, S., Bots, P., Roncal-Herrero, T., and Benning, L. G.: The role of pH and Mg on the stability and crystallization of amorphous calcium carbonate, J. Alloy. Compd., 536, S477–S479, https://doi.org/10.1016/j.jallcom.2011.11.057, 2012.

Rollion-Bard, C. and Erez, J.: Intra-shell boron isotope ratios in benthic foraminifera: Implications for paleo-pH reconstructions, Geochim. Cosmochim. Ac., 74, 1530–1536, 2010.

Saulnier, S., Rollion-Bard, C., Vigier, N., and Chaussidon, M.: Mg isotope fractionation during calcite precipitation: An experimental study, Geochim. Cosmochim. Ac., 91, 75–91, https://doi.org/10.1016/j.gca.2012.05.024, 2012.

Schiff, J. A.: Pathways of Assimilatory Sulphate Reduction in Plants and Microorganisms, in: Ciba Foundation Symposium 72 – Sulphur in Biology, 49–69, https://doi.org/10.1002/9780470720554.ch4, 1980.

Seknazi, E., Kozachkevich, S., Polishchuk, I., Bianco Stein, N., Villanova, J., Suuronen, J.-P., Dejoie, C., Zaslansky, P., Katsman, A., and Pokroy, B.: From spinodal decomposition to alternating layered structure within single crystals of biogenic magnesium calcite, Nat. Commun., 10, 4559, https://doi.org/10.1038/s41467-019-12168-8, 2019.

Sim, M. S., Woo, D. K., Kim, B., Jeong, H., Joo, Y. J., Hong, Y. W., and Choi, J. Y.: What Controls the Sulfur Isotope Fractionation during Dissimilatory Sulfate Reduction?, ACS Environ. Au, 3, 76–86, https://doi.org/10.1021/acsenvironau.2c00059, 2023.

Spero, H. J.: Life history and stable isotope geochemistry of planktonic foraminifera, The Paleontological Society Papers, 4, 7–36, 1998.

Spero, H. J., Eggins, S. M., Russell, A. D., Vetter, L., Kilburn, M. R., and Hönisch, B.: Timing and mechanism for intratest Mg/Ca variability in a living planktic foraminifer, Earth Planet. Sc. Let., 409, 32–42, https://doi.org/10.1016/j.epsl.2014.10.030, 2015a.

Spero, H. J., Eggins, S. M., Russell, A. D., Vetter, L., Kilburn, M. R., and Hönisch, B.: Timing and mechanism for intratest Mg/Ca variability in a living planktic foraminifer, Earth Planet. Sc. Let., 409, 32–42, https://doi.org/10.1016/j.epsl.2014.10.030, 2015b.

Tanaka, K., Okaniwa, N., Miyaji, T., Murakami-Sugihara, N., Zhao, L., Tanabe, K., Schöne, B. R., and Shirai, K.: Microscale magnesium distribution in shell of the Mediterranean mussel Mytilus galloprovincialis: An example of multiple factors controlling Mg/Ca in biogenic calcite, Chem. Geol., 511, 521–532, https://doi.org/10.1016/j.chemgeo.2018.10.025, 2019.

ten Kuile, B. and Erez, J.: Uptake of inorganic carbon and internal carbon cycling in symbiont-bearing benthonic foraminifera, Mar. Biol., 94, 499–509, https://doi.org/10.1007/BF00431396, 1987.

ter Kuile, B. and Erez, J.: The size and function of the internal inorganic carbon pool of the foraminifer Amphistegina lobifera, Mar. Biol., 99, 481–487, https://doi.org/10.1007/BF00392555, 1988.

Thaler, C., Paris, G., Dellinger, M., Dissard, D., Berland, S., Marie, A., Labat, A., and Bartolini, A.: Impact of seawater sulfate concentration on sulfur concentration and isotopic composition in calcite of two cultured benthic foraminifera, Biogeosciences, 20, 5177–5198, https://doi.org/10.5194/bg-20-5177-2023, 2023.

The Cenozoic CO_2 Proxy Integration Project (CenCO2PIP) Consortium, Hönisch, B., Royer, D. L., Breecker, D. O., Polissar, P. J., Bowen, G. J., Henehan, M. J., Cui, Y., Steinthorsdottir, M., McElwain, J. C., Kohn, M. J., Pearson, A., Phelps, S. R., Uno, K. T., Ridgwell, A., Anagnostou, E., Austermann, J., Badger, M. P. S., Barclay, R. S., Bijl, P. K., Chalk, T. B., Scotese, C. R., de la Vega, E., DeConto, R. M., Dyez, K. A., Ferrini, V., Franks, P. J., Giulivi, C. F., Gutjahr, M., Harper, D. T., Haynes, L. L., Huber, M., Snell, K. E., Keisling, B. A., Konrad, W., Lowenstein, T. K., Malinverno, A., Guillermic, M., Mejía, L. M., Milligan, J. N., Morton, J. J., Nordt, L., Whiteford, R., Roth-Nebelsick, A., Rugenstein, J. K. C., Schaller, M. F., Sheldon, N. D., Sosdian, S., Wilkes, E. B., Witkowski, C. R., Zhang, Y. G., Anderson, L., Beerling, D. J., Bolton, C., Cerling, T. E., Cotton, J. M., Da, J., Ekart, D. D., Foster, G. L., Greenwood, D. R., Hyland, E. G., Jagniecki, E. A., Jasper, J. P., Kowalczyk, J. B., Kunzmann, L., Kürschner, W. M., Lawrence, C. E., Lear, C. H., Martínez-Botí, M. A., Maxbauer, D. P., Montagna, P., Naafs, B. D. A., Rae, J. W. B., Raitzsch, M., Retallack, G. J., Ring, S. J., Seki, O., Sepúlveda, J., Sinha, A., Tesfamichael, T. F., Tripati, A., van der Burgh, J., Yu, J., Zachos, J. C., and Zhang, L.: Toward a Cenozoic history of atmospheric CO_2, Science, 382, eadi5177, https://doi.org/10.1126/science.adi5177, 2023.

Timofeeff, M. N., Lowenstein, T. K., Brennan, S. T., Demicco, R. V., Zimmermann, H., Horita, J., and Von Borstel, L. E.: Evaluating seawater chemistry from fluid inclusions in halite: examples from modern marine and nonmarine environments, Geochim. Cosmochim. Ac., 65, 2293–2300, 2001.

Tostevin, R., Turchyn, A. V., Farquhar, J., Johnston, D. T., Eldridge, D. L., Bishop, J. K. B., and McIlvin, M.: Multiple sulfur isotope constraints on the modern sulfur cycle, Earth Planet. Sc. Let., 396, 14–21, https://doi.org/10.1016/j.epsl.2014.03.057, 2014.

Tung, M. S.: Calcium Phosphates: Structure, Composition, Solubility, and Stability, in: Calcium Phosphates in Biological and Industrial Systems, edited by: Amjad, Z., vol. 7, Springer, Boston, MA, https://doi.org/10.1007/978-1-4615-5517-9_1, 1998.

Tyszka, J., Godos, K., Goleń, J., and Radmacher, W.: Foraminiferal organic linings: Functional and phylogenetic challenges, Earth-Sci. Rev., 220, 103726, https://doi.org/10.1016/j.earscirev.2021.103726, 2021.

van Dijk, I., de Nooijer, L. J., Boer, W., and Reichart, G.-J.: Sulfur in foraminiferal calcite as a potential proxy for seawater carbonate ion concentration, Earth Planet. Sc. Let., 470, 64–72, https://doi.org/10.1016/j.epsl.2017.04.031, 2017.

van Dijk, I., Mouret, A., Cotte, M., Le Houedec, S., Oron, S., Reichart, G.-J., Reyes-Herrera, J., Filipsson, H. L., and Barras, C.: Chemical Heterogeneity of Mg, Mn, Na, S, and Sr in Benthic Foraminiferal Calcite, Front. Earth Sci., 7, https://doi.org/10.3389/feart.2019.00281, 2019a.

van Dijk, I., Barras, C., de Nooijer, L. J., Mouret, A., Geerken, E., Oron, S., and Reichart, G.-J.: Coupled calcium and inorganic carbon uptake suggested by magnesium and sulfur incorporation in foraminiferal calcite, Biogeosciences, 16, 2115–2130, https://doi.org/10.5194/bg-16-2115-2019, 2019b.

Weiner, S. and Addadi, L.: Crystallization pathways in biomineralization, Annu. Rev. Mater. Res., 41, 21–40, 2011.

Weiner, S. and Erez, J.: Organic matrix of the shell of the foraminifer, Heterostegina depressa, J. Foramin. Res., 14, 206–212, https://doi.org/10.2113/gsjfr.14.3.206, 1984.

Weiner, S., Levi-Kalisman, Y., Raz, S., and Addadi, L.: Biologically Formed Amorphous Calcium Carbonate, Connect. Tissue Res., 44, 214–218, https://doi.org/10.1080/03008200390181681, 2003.

Zhang, H., Xu, B., Lai, Z., Paytan, A., Burnett, W. C., Guo, X., Ren, L., Lu, Y., Zhang, J., Yuan, H., Yao, Q., and Yu, Z.: Phosphorus-to-calcium ratios in benthic foraminiferal shells as a proxy for coastal seawater phosphate concentrations, Earth Planet. Sc. Let., 654, 119210, https://doi.org/10.1016/j.epsl.2025.119210, 2025.

Zou, Z., Xie, J., Macías-Sánchez, E., and Fu, Z.: Nonclassical Crystallization of Amorphous Calcium Carbonate in the Presence of Phosphate Ions, Cryst. Growth Des., 21, 414–423, https://doi.org/10.1021/acs.cgd.0c01245, 2021.